Dendrites of DG granule cells contribute to pattern separation by controlling sparsity

Spyridon Chavlis[1, 2], Panagiotis C. Petrantonakis[1], Panayiota Poirazi[1]

[1]Institute of Molecular Biology and Biotechnology (IMBB), Foundation for Research and Technology – Hellas (FORTH), Heraklion, Crete

[2]Department of Biology, School of Sciences and Engineering, University of Crete, Heraklion, Crete

1

8 Abstract

9 The hippocampus plays a key role in pattern separation, the process of transforming similar

10 incoming information to highly dissimilar, non-overlapping representations. Sparse firing

11 granule cells (GCs) in the dentate gyrus (DG) have been proposed to undertake this

12 computation, but little is known about which of their properties influence pattern separation.

13 Dendritic atrophy has been reported in diseases associated with pattern separation deficits,

14 suggesting a possible role for dendrites in this phenomenon. To investigate whether and

15 how the dendrites of GCs contribute to pattern separation, we build a simplified, biologically

16 relevant, computational model of the DG. Our model suggests that the presence of GC

17 dendrites is associated with high pattern separation efficiency while their atrophy leads to

18 increased excitability and performance impairments. These impairments can be rescued by

19 restoring GC sparsity to control levels through various manipulations. We predict that

20 dendrites contribute to pattern separation as a mechanism for controlling sparsity.

Introduction

The hippocampus is known to be involved in memory formation, storage and consolidation (Squire et al., 2004), but its specific functionalities remain a mystery. One such functionality is the ability to rapidly store non-overlapping representations of similar inputs and thereafter, retrieve them given a partial or noisy stimulus. Theoretical models refer to those processes as pattern separation and pattern completion, respectively (Marr, 1971; Treves and Rolls, 1994; Yassa and Stark, 2011; Santoro, 2013). The Dentate Gyrus (DG), in particular, has been proposed to implement pattern separation by sparsifying and orthogonalizing its input, coming mainly from the Entorhinal Cortex (EC), and thereafter, projecting this information to the CA3 area via the mossy fibers (Treves and Rolls, 1994). DG has been hypothesized to separate two distinct but overlapping patterns through the activation of different Granule Cells (GCs), through the expression of different firing rates in identical neuronal populations (Deng et al., 2010) or a combination of the two. While several studies have investigated pattern separation both in rodents (Leutgeb et al., 2004, 2005, 2007) and humans (Kirwan and Stark, 2007; Bakker et al., 2008; Lacy et al., 2011; Motley and Kirwan, 2012), the role of dendrites in this phenomenon remains unknown.

The DG is the first subregion of the hippocampus that receives incoming information from other brain areas. DG principal neurons, the Granule Cells (GCs), receive input from excitatory afferents coming from EC layer II cells and project to the CA3 subregion. In addition, they receive input from other DG excitatory cells, the Mossy Cells (MCs), and various interneurons (Sik et al., 1997) with Basket Cells (BCs) and Hilar Perforant Path associated (HIPP) cells being the most important. MCs form an inhibitory circuit as their axons contact the BCs. The net effect of MC excitation to both GCs and BCs is considered to be inhibitory (Jinde et al., 2012).

Experimental studies have shown that only a small population of GCs, ~5%, are active in a single context (Marrone et al., 2011; Satvat et al., 2011; Danielson et al., 2016), a

47 phenomenon termed sparse coding (Olshausen and Field, 2004). It has been proposed that

48 sparse coding in GCs enhances pattern separation by recruiting different subgroups of GCs

49 to encode similar incoming stimuli (Treves et al., 2008; Petrantonakis and Poirazi, 2014,

50 2015). Computational models (Santhakumar et al., 2005; Yim et al., 2015) and experimental

51 studies (Nitz and McNaughton, 2004; Jinde et al., 2012) have proposed that inhibition

52 controls GC activity which, in turn, mediates pattern separation (Myers and Scharfman,

53 2009, 2011; Ikrar et al., 2013; Faghihi and Moustafa, 2015).

54 The ability to perform pattern separation is critical for normal brain functioning and its

55 impairment is associated with cognitive decline. Diseases such as schizophrenia (Das et al.,

56 2014) and Alzheimer's Disease (AD) (Ally et al., 2013), where cognitive decline is evident,

57 are both characterized by pattern separation deficiencies. Interestingly, these conditions are

58 also characterized by alterations in the anatomical properties of GC dendrites, such as a

59 decrease in the total dendritic length (Einstein et al., 1994) and spine loss (Jain et al., 2012).

60 Dendritic growth on the other hand has been associated with pattern separation

61 enhancements. Specifically, voluntary running was recently shown to enhance pattern

62 separation and this enhancement was attributed to an increase in the neurogenesis rate that

63 was accompanied by increased GC dendrite outgrowth in active compared to sedentary

64 animals (Bolz et al., 2015). These findings suggest that the dendrites of GCs are likely to

65 play a key role in pattern separation mediated by the DG.

66 To investigate this possibility, we implemented a morphologically simple, yet biologically

67 relevant, scaled-down spiking neural network model of the DG. The model consists of four

68 types of cells (MCs, BCs, HIPP and GCs) modeled as simplified integrate-and-fire neurons.

69 The GC model alone was extended to incorporate dendrites. The electrophysiological

70 properties of all cell types were calibrated according to a range of experimental data. An

71 advantage of using such a simplified approach lies in the small number of parameters that

72 make it possible to characterize their role in the behavior of the model. Despite its simplicity,

73 the model exhibits realistic pattern separation under several conditions and explains how

74   inhibition to GCs provided directly from BCs and indirectly via the inhibitory circuitry through

75   MCs impact this task, as suggested by a number of recent studies (Myers and Scharfman,

76   2011; Jinde et al., 2012), thus, supporting its biological relevance. We use the model to

77   investigate whether and how GC dendrites may contribute to pattern separation.

Results

The Dentate Gyrus model

The DG network model consists of four different neuronal types, namely GCs, BCs, MCs, and HIPP cells. MCs, BCs and HIPP cells are modeled as adaptive exponential I&F (aEIF) point neurons (Brette and Gerstner, 2005). GCs consist of a leaky integrate-and-fire somatic compartment connected to a variable number of active dendritic compartments (3, 6 or 12) whose morphology relies loosely on anatomical data (see Materials and Methods). I&F models were selected primarily because of their correspondence with experimental parameters (e.g. the C_m, R_m, R_{in}) that facilitated constraining with experimental data. Since dentate GCs are known to have 10-15 dendrites (Claiborne et al., 1990), we consider the GC model with 12 dendrites as the control. A schematic illustration of the DG network is shown in Figure 1A.

All computational neuron models were validated against experimental data with respect to their activity and basic electrophysiological properties (Lübke et al., 1998; Bartos et al., 2001; Krueppel et al., 2011). The spiking profiles of the four neuronal model types are depicted in Figure 2 while the respective I-V and I-F curves compared against experimental data are shown in Figure 2-figure supplement 1 and Figure 2-figure supplement 2. The control (12-dendrite) GC model was validated against the experimental data of (Krueppel et al., 2011) with respect to its dendritic input-output function, which was found to be slightly above linearity (see Figure 2-figure supplement 3(A)). Table 1 lists the model and experimental values of basic intrinsic properties for each of these cell types. Overall, the electrophysiological properties of the computational models of neurons included in the DG network are in fair alignment with experimental findings. It should be noted that spiking profiles are not taken into account when estimating pattern separation in the DG network model. A GC model neuron was considered active even if it produced a single spike. Thus, we chose to fit average values rather than temporal profiles of the model neurons.

Pattern separation in the DG model

Following validation of the individual neuron models, we tested the DG network's ability to implement pattern separation when presented with pairs of inputs characterized by various degrees of similarity (modeled as overlap in the two activated EC populations). An example of two such input patterns and their corresponding output is schematically illustrated in Figure 1B. The network model is deemed capable of separating similar input patterns if the value of a distance metric f is substantially larger in the DG output (GC activity) compared to its input (EC cell activity). Pattern separation is primarily estimated by looking at the differences in the populations of neurons that encode each input ('population distance', f_1). To account for the possibility of rate-based pattern separation (Deng et al., 2010), we also simulate the network under conditions where the two input pairs are identical in terms of EC 'population distance' (i.e., $f_{1(input)} = 0$) but differ in their mean firing rates (graphically depicted in Figure 1C). Pattern separation in this case is measured by looking at differences in the average firing rate of the neurons encoding both inputs ('rate distance', f_2). The 'rate distance' is estimated both at the input (EC cells) and the output (GCs) levels (see Materials and Methods). Pattern separation is successfully performed if the 'rate distance' of the output ($f_{2(output)}$) is larger than that of the input ($f_{2(input)}$). The network's ability to perform pattern separation across all (200) input pairs measured with both metrics is shown in Table 2. These results demonstrate that two inputs that are quite similar in their topology (i.e., originate largely (f_1) or entirely from the same neurons, perhaps with different firing rates (f_2)), induce substantially different activation patterns of the GCs that they impinge on (outputs) in the DG network.

Understanding the role of Inhibition in Pattern separation

After establishing the network's ability to perform pattern separation, we tested its validity against experimental data with respect to the role of inhibition in this phenomenon. The network model reproduced the recent findings of Engin et al., whereby inhibition exerted by

7

130　　BCs was critical for the sparse firing of GCs (Engin et al., 2015). Specifically, removal of all

131　　BCs resulted in an over-excitation of the GC model population (more than 50% of GCs

132　　responded strongly to any input). This over-excitation in turn impaired pattern separation, as

133　　the GC populations responding to the two inputs became nearly identical and fired at very

134　　similar, high frequencies. These findings are also in line with experimental evidence

135　　reporting increased memory interference under conditions of reduced BC activity (Engin et

136　　al., 2015).

137　　Since MCs have also been suggested to control the excitability of DG granule cells (Jinde et

138　　al., 2013), we simulated a complete MC-loss lesion (Figure 3A) as per (Ratzliff et al., 2004).

139　　This manipulation led to an increase in the proportion of active GCs for all input patterns

140　　tested (Figure 3B, 3D), and a decrease in pattern separation efficiency, measured either with

141　　the population (f_1, Figure 3C) (Wilcoxon test, $W_1=2095.5$, $p_1{\approx}10^{-9}$, 95% CI_1 [0.05, 0.09],

142　　$W_2=2242.0$, $p_2{\approx}10^{-11}$, 95% CI_2 [0.06, 0.10], $W_3=2363.0$, $p_3{\approx}10^{-11}$, 95% CI_3 [0.07, 0.11],

143　　$W_4=2444.0$, $p_4{\approx}10^{-16}$, 95% CI_4 [0.08, 0.12]) or rate metrics (f_2, Figure 3E) (Wilcoxon test,

144　　$W=930.0$, $p=0.0276$, 95% CI [0.01, 0.07]). The subscripts (form one to four) in the Wilcoxon

145　　test statistic (W), p-value, confidence interval (CI) correspond to the four experiments with

146　　different input overlaps (see Materials and Methods). The observed decrease in sparsity

147　　under the MC-loss condition was accompanied by small increases in the excitability levels of

148　　GC models. Specifically, for the population coding experiment, the mean GC firing frequency

149　　increased from 3.5 Hz to 4.82 Hz, while for the rate-based coding experiment from 3.75 Hz

150　　to 4.94 Hz for 40 Hz inputs and from 5.24 Hz to 8.07 Hz for 50 Hz inputs. These findings are

151　　in line with the experimental data of (Ratzliff et al., 2004) where MC-loss did not lead to an

152　　over-excitation of GCs.

153　　Taken together, the proposed DG network model a) exhibits single-neuron response

154　　properties that are in good agreement with experimental data, b) implements a connectivity

155　　profile that relies on experimental observations, c) exhibits robust pattern separation and d)

156　　replicates experimental data about the role of BCs and MC cells in the aforementioned task.

157 These features support the biological plausibility of the model which is next used to

158 investigate how dendrites contribute to pattern separation.

Dendrites and Pattern separation

Dendritic pruning

161 The main question of interest in this work is whether and how dendrites may contribute to

162 pattern separation. To answer this question we started by examining whether the number of

163 dendrites correlates with pattern separation performance as we prune the GC (sister)

164 branches from 12 (control) to 6 and 3 (Figure 4A). To assess the effect of dendritic number,

165 we kept all other parameters (maximum dendritic length, dendritic diameter in the IML, MML

166 and OML layers, membrane capacitance, "leak" conductance, number of activated synapses

167 and input firing rates) of the three GC models identical to those of the control. Dendritic

168 integration properties for the pruned GC models are shown in Figure 2-figure supplement 3

169 (B). The control DG network (12-dendrite model) was calibrated to have a mean population

170 sparsity level of 2-5% as per (Treves et al., 2008; Danielson et al., 2016), meaning that only

171 a small fraction of GCs were active for any given stimulus.

172 Interestingly, pattern separation of pairs of inputs with increasing similarity (measured either

173 by population distances, Figure 4C, or by rate distances, Figure 4E) was successfully

174 performed in the control as well as both pruned models for all pairs of inputs tested. The

175 efficiency of pattern separation however correlated with the number of dendrites in GCs

176 (Figure 4C, 4E), with the 12-dendrite GC model achieving the best performance for both

177 population (12-dendrite vs. 6-dendrite: Wilcoxon test, $W_1=1849.0$, $p_1\approx10^{-5}$, 95% CI_1 [0.02,

178 0.06], $W_2=1818.5$, $p_2\approx10^{-4}$, 95% CI_2 [0.02, 0.06], $W_3=2060.5$, $p_3\approx10^{-8}$, 95% CI_3 [0.04, 0.07],

179 $W_4=1948.0$, $p_4\approx10^{-6}$ 95% CI_4 [0.03, 0.06] and 12-dendrite vs. 3-dendrite: Wilcoxon test,

180 $W_1=2471.0$, $p_1\approx10^{-16}$, 95% CI_1 [0.11, 0.15], $W_2=2462.0$, $p_2\approx10^{-16}$, 95% CI_2 [0.11, 0.14],

181 $W_3=2473.0$, $p_3\approx10^{-16}$, 95% CI_3 [0.10, 0.13], $W_4=2451.0$, $p_4\approx10^{-16}$, 95% CI_4 [0.08, 0.11]) and

182 rate based-metrics (12-dendrite vs. 6-dendrite: Wilcoxon test, $W=1764.0$, $p=0.0004$, 95% CI

183   *[0.03, 0.09] and 12-dendrite vs. 3-dendrite: Wilcoxon test, W=2072.0, p≈10^{-8}, 95% CI [0.06,*

184   *0.12])* (i.e., the highest $f_{1(output)}$ and $f_{2(output)}$, respectively).

185   These findings are better understood by looking at the sparsity levels exhibited by the three

186   GC network models. As shown in Figure 4B, the percentage of active GCs for the

187   population-based experiment increased substantially when the number of dendrites was

188   reduced. It rose from ~5%, to ~10% and ~20%, for GC model cells with 12, 6 and 3

189   dendrites, respectively. These differences in activity distributions were statistically significant

190   (12-dendrite vs. 6-dendrite: Kolmogorov-Smirnov test, *D=1.000, p≈10^{-16}* and 12-dendrite vs.

191   3-dendrite: Kolmogorov-Smirnov test, *D=1.000. p≈10^{-16}*). The activity levels of the three

192   models followed a similar pattern in the case of rate-based coding (Figure 4D); Input

193   patterns with high firing rates induced lower sparsity levels in the 12-dendrite GC model,

194   followed by the 6-dendrite model and then the 3-dendrite model (12-dendrite vs. 6-dendrite:

195   Kolmogorov-Smirnov test, *D=1.000, p≈10^{-16}* and 12-dendrite vs. 3-dendrite: Kolmogorov-

196   Smirnov test, *D=1.000. p≈10^{-16}*). These data reveal that high levels of sparsity (namely low

197   levels of GC activity) and pattern separation efficiency in the network model are a direct

198   consequence of having multiple dendrites and suggest that dendrites may contribute to

199   pattern separation through their effects on sparsity.

200   **Dendritic growth**

201   To further test whether the presence of dendrites helps pattern separation by increasing

202   sparsity, we also simulated the opposite process, namely the growth of dendrites. We built

203   GC models with 3, 6 and 12 dendrites with shapes that roughly mimic the stages of dendritic

204   growth (Figure 5A): starting with a GC model consisting of 3 thick dendritic compartments

205   and adding a branch point with two thinner sister branches at each terminal dendrite we end

206   up with a 12-dendrite model which is identical with our control one (see Materials and

207   Methods). Dendritic integration properties for the growth GC models are shown in Figure 2-

208   figure supplement 3 (C). Note that in this simulation, the number, length and mean diameter

209   of dendrites differ between the three models.

210   In line with the findings of the pruning experiment, the percentage of active GCs declined as

211   the number of dendrites increased (Figure 5B,D). The average GC activity for the

212   population-coding experiment started at ~70% for the network with 3 GC dendrites, dropped

213   to ~28% for the network with 6 GC dendrites and to ~5% for the 12-dendrite (control) model

214   (all differences were statistically significant, (12-dendrite vs. 6-dendrite: Kolmogorov-Smirnov

215   test, $D=1.000$, $p{\approx}10^{-16}$ and 12-dendrite vs. 3-dendrite: Kolmogorov-Smirnov test, $D=1.000$.

216   $p{\approx}10^{-16}$). Similar differences in GC sparsity were seen in the rate-based experiment (Figure

217   5D). In both cases, the 3-dendrite model exhibited much higher activity levels than the ones

218   seen in the pruning experiment (Figure 4B,D), primarily because of additional alterations in

219   dendritic length and diameter. Moreover, pattern separation measured by the population

220   metric was completely impaired in the 3-dendrite model (Figure 5C, blue line falls below the

221   diagonal) while performance based on rate coding remained above baseline (Figure 5E, blue

222   bar). Pattern separation was successfully performed in the 6-dendrite model albeit with lower

223   efficiency compared to the 12-dendrite model, as evaluated both with the population (12-

224   dendrite vs. 6-dendrite: Wilcoxon test, $W_1=2456.0$, $p_1{\approx}10^{-16}$, 95% CI_1 [0.12, 0.15],

225   $W_2=2421.0$, $p_2{\approx}10^{-15}$, 95% CI_2 [0.09, 0.13], $W_3=2466.0$, $p_3{\approx}10^{-16}$, 95% CI_3 [0.09, 0.13],

226   $W_4=2368.0$, $p_4{\approx}10^{-14}$, 95% CI_4 [0.06, 0.09] and 12-dendrite vs. 3-dendrite: Wilcoxon test, W_{1-}

227   $_4=2500.0$, $p_{1-4}{\approx}10^{-16}$, 95% CI_1 [0.44, 0.48], 95% CI_2 [0.40, 0.43], 95% CI_3 [0.36, 0.39], 95%

228   CI_4 [0.29, 0.32],) and rate distance metrics (12-dendrite vs. 6-dendrite: Wilcoxon test,

229   $W=1638.0$, $p=0.0076$, 95% CI [0.01, 0.07] and 12-dendrite vs. 3-dendrite: Wilcoxon test,

230   $W=2305.0$, $p{\approx}10^{-13}$, 95% CI [0.17, 0.25]) (Figure 5C,E).

231   Taken together, the "pruning" and "growth" simulations suggest a strong link between pattern

232   separation efficiency and GC population sparsity (Aimone et al., 2011, Deng et al., 2010)

233   and predict that dendrites may serve as a mechanism for increasing the sparsity of the GC

234   population which in turn enhances pattern separation.

Controlling sparsity with non-dendritic mechanisms

236   The above simulations predict that dendrites can be sufficient for mediating sparsity, which

237   in turn enhances pattern separation. We next ask whether they are necessary for this task,

238   as it is possible that a GC neuron can counteract the decrease in sparsity induced by having

239   fewer/shorter dendrites through alternative mechanisms.

240   *Input resistance* **does** *not explain differences in sparsity or pattern separation*

241   *efficiency*

242   First, we assessed the effect of input resistance differences among the various GC models

243   on sparsity and pattern separation efficiency. A possible explanation of the above findings is

244   that a GC model with a small dendritic tree has increased input resistance (as can be seen

245   in Supplementary file 1A) which in turn leads to higher excitability and decreased sparsity.

246   We thus corrected the input resistance in the 6- and 3-dendrite models to match the one in

247   the 12-dendrite model (at the soma) by modifying a) the "leak" channel conductance (g_{leak})

248   or b) the size of the somatic compartments (see Supplementary file 1B for the corrected

249   values and Figure 2-figure supplement 4 for the corrected dendritic integration profiles).

250   Specifically, for the pruning models, g_{leak} increased by *1.230* and *1.635* for the 6- and 3-

251   dendrite models while for the growth models, these numbers were *1.596* and *2.438*,

252   respectively. Figure 6 shows the outcome of this correction for both pruning (A-B) and

253   growth (C-D) cases. As evident from the figure, correcting the input resistance by increasing

254   the "leak" conductance in the pruning case, reduced but did not eliminate differences in

255   sparsity (Figure 6A) (12-dendrite vs. 6-dendrite: Kolmogorov-Smirnov test, *D=0.868, p≈10^{-16}*

256   and 12-dendrite vs. 3-dendrite: Kolmogorov-Smirnov test, *D=1.000. p≈10^{-16}*) or pattern

257   separation efficiency (Figure 6B) (12-dendrite vs. 6-dendrite: Wilcoxon test, *W_1=1636.5,*

258   *p_1=0.0078, 95% CI_1 [0.01, 0.07], W_2=1606.5, p_2=0.0141, 95% CI_1 [0.01, 0.04], W_3=1732.5,*

259   *p_3=0.0009, 95% CI_1 [0.02, 0.05], W_4=1668.5, p_4=0.0040 95% CI_4 [0.01, 0.04]* and 12-

260   dendrite vs. 3-dendrite: Wilcoxon test, *W_1=2164.0, p_1≈10^{-10}, 95% CI_1 [0.06, 0.09],*

261 $W_2=2177.5$, $p_2≈10^{-10}$, 95% CI_2 [0.05, 0.09], $W_3=2284.0$, $p_3≈10^{-12}$, 95% CI_3 [0.06, 0.09],

262 $W_4=2151.0$, $p_4≈10^{-10}$ 95% CI_4 [0.04, 0.07]). Similar findings were seen in the growth case,

263 both for the sparsity (Figure 6C) (12-dendrite vs. 6-dendrite: Kolmogorov-Smirnov test,

264 $D=0.956$, $p≈10^{-16}$ and 12-dendrite vs. 3-dendrite: Kolmogorov-Smirnov test, $D=1.000$, $p≈10^{-16}$

265) and pattern separation efficiency (Figure 6D) (12-dendrite vs. 6-dendrite: Wilcoxon test,

266 $W_1=2252.5$, $p_1≈10^{-12}$, 95% CI_1 [0.06, 0.10], $W_2=2387.0$, $p_2≈10^{-15}$, 95% CI_2 [0.09, 0.12],

267 $W_3=2408.5$, $p_3≈10^{-15}$, 95% CI_3 [0.07, 0.11], $W_4=2258.5$, $p_4≈10^{-12}$, 95% CI_4 [0.05, 0.08] and

268 12-dendrite vs. 3-dendrite: Wilcoxon test, $W_{1-4}=2500.0$, $p_{1-4}≈10^{-16}$, 95% CI_1 [0.24, 0.28], 95%

269 CI_2 [0.22, 0.26], 95% CI_3 [0.20, 0.24], 95% CI_4 [0.16, 0.19]). Both sparsity and pattern

270 separation efficiency were highest in the 12-dendrite, followed by the 6-dendrite and the 3-

271 dendrite models. The same was seen when using the rate-based distance metric to evaluate

272 sparsity and pattern separation (Figure 6-figure supplement 1). In all cases, differences were

273 more pronounced in the growth compared to the pruning case, in line with the findings of

274 Figures 4-5.

275 Similar results were obtained when correcting the input resistance by increasing the

276 dimensions of the somatic compartment (Supplementary file 1B). For the pruning models,

277 the soma increased by a factor of *1.278* and *1.527* in the 6- and 3-dendrite models,

278 respectively while for the growth models, these factors were *1.513* and *1.746*, respectively.

279 As shown in Figure 7 (A-B), for the pruning case, differences in sparsity (12-dendrite vs. 6-

280 dendrite: Kolmogorov-Smirnov test, $D=0.820$, $p≈10^{-16}$ and 12-dendrite vs. 3-dendrite,

281 Kolmogorov-Smirnov test, $D=1.000$, $p≈10^{-16}$) and pattern separation efficiency (12-dendrite

282 vs. 6-dendrite: Wilcoxon test, $W_1=1420.5$, $p_1=0.2412$, 95% CI_1 [-0.01, 0.03], $W_2=1588.0$,

283 $p_2=0.0020$, 95% CI_2 [0.01, 0.04], $W_3=1713.5$, $p_3=0.0014$, 95% CI_3 [0.02, 0.05], $W_4=1600.5$,

284 $p_4=0.0158$, 95% CI_1 [0.01, 0.04] and 12-dendrite vs. 3-dendrite: Wilcoxon test, $W_1=1914.0$,

285 $p_1≈10^{-6}$, 95% CI_1 [0.03, 0.07], $W_2=1878.0$, $p_2≈10^{-5}$, 95% CI_2 [0.02, 0.06], $W_3=1979.5$, $p_3≈10^{-7}$,

286 95% CI_3 [0.03, 0.07], $W_4=1891.5$, $p_4≈10^{-5}$, 95% CI_4 [0.02, 0.05]) among corrected models

287 decreased significantly but were not eliminated. Similar findings were seen in the growth

288   case, both for the sparsity (12-dendrite vs. 6-dendrite: Kolmogorov-Smirnov test, $D=1.000$,

289    $p \approx 10^{-16}$ and 12-dendrite vs. 3-dendrite: Kolmogorov-Smirnov test, $D=1.000$, $p \approx 10^{-16}$) and

290   pattern separation efficiency (12-dendrite vs. 6-dendrite: Wilcoxon test, $W_1=1965.0$, $p_1 \approx 10^{-13}$,

291   95% CI_1 [0.04, 0.08], $W_2=1961.5$, $p_2 \approx 10^{-6}$, 95% CI_2 [0.03, 0.07], $W_3=2112.5$, $p_3 \approx 10^{-9}$, 95% CI_3

292   [0.04, 0.08], $W_4=1919.5$, $p_4 \approx 10^{-6}$, 95% CI_4 [0.02, 0.06] and 12-dendrite vs. 3-dendrite:

293   Wilcoxon test, $W_1=2465.0$, $p_1 \approx 10^{-16}$ 95% CI_1 [0.12, 0.15], $W_2=2463.0$, $p_2 \approx 10^{-16}$, 95% CI_2

294   [0.10, 0.14], $W_3=2470.0$, $p_3 \approx 10^{-16}$, 95% CI_3 [0.09, 0.12], $W_4=2388.0$, $p_4 \approx 10^{-15}$95% CI_4 [0.07,

295   0.10]) .Both sparsity and pattern separation efficiency remained highest in the 12-dendrite,

296   followed by the 6-dendrite and the 3-dendrite models. Similar findings were obtained when

297   using the rate-based distance metric to assess pattern separation (Figure 7-figure

298   supplement 1). Note that correcting the input resistance via increasing the somatic

299   compartment is more effective than increasing the leak conductance, as both C_m and g_{leak}

300   increase proportionally, keeping the membrane time constant identical across model cells.

301   Overall, these simulations suggest that while the input resistance is a key determinant of GC

302   neuron activity, it does not fully explain the differences in sparsity and pattern separation

303   efficiency among models with 3, 6 or 12 GC dendrites.

304   ***Sparsity is the key determinant of pattern separation efficiency***

305   The question that arises naturally from the above findings is whether further manipulations of

306   the leak conductance and/or somatic dimensions could match sparsity across all models?

307   Moreover, would matching sparsity result in identical pattern separation efficiency, thus

308   making sparsity the key determinant of pattern separation (O'Reilly and McClelland, 1994;

309   Johnston et al., 2015)? To answer these questions we explored the effects of manipulating

310   intrinsic (g_{leak} and somatic dimensions) as well as extrinsic (synaptic weight) mechanisms in

311   the 3-, 6- and 12-dendrite GC models. Due to the consistent nature of the previous results,

312   the remaining simulations were performed using the pruning experiment configuration to

313   generate the 3- and 6-dendrite GC models and the population-based metric to assess

14

314   pattern separation. Their corresponding properties are shown in Supplementary file 1C and

315   the corrected dendritic integration profiles in Figure 2-figure supplement 5.

316   As shown in Figure 8Ai, increasing g_{leak} by a factor of *1.58* and *2.48*, in the 6- and 3-dendrite

317   GC models respectively, eliminated the differences in sparsity distributions compared to the

318   control (12-dendrite vs. 6-dendrite: Kolmogorov-Smirnov test, *D=0.096, p=0.1995* and 12-

319   dendrite vs. 3-dendrite: Kolmogorov-Smirnov test, *D=0.100, p=0.1641*). The same was

320   observed with respect to pattern separation efficiency (Figure 8Aii). All three models

321   exhibited identical performance across all difficulty levels (12-dendrite vs. 6-dendrite:

322   Wilcoxon test, *W_1=1148.5, p_1=0.4863, 95% CI_1 [-0.03, 0.01], W_2=1263.5, p_2=0.9286, 95%*

323   *CI_2 [-0.02, 0.02], W_3=1337.5, p_3=0.5486, 95% CI_3 [-0.01, 0.02], W_4=1192.0, p_4=0.6918, 95%*

324   *CI_4 [-0.02, 0.02]*, 12-dendrite vs. 3-dendrite: Wilcoxon test, *W_1=1195.5, p_1=0.7097, 95% CI_1*

325   *[-0.03, 0.01], W_2=1067.5, p_2=0.2096, 95% CI_2 [-0.04, 0.01], W_3=1326.5, p_3=0.6003, 95% CI_3*

326   *[-0.01, 0.02], W_4=1246.5, p_4=0.9835, 95% CI_4 [-0.02, 0.02]*). Similarly, increasing the

327   diameter and length of the somatic compartment in the 6- and 3-dendrite models by *1.480*

328   and *1.870*, respectively (Figure 8Bi) resulted in similar sparsity (12-dendrite vs. 6-dendrite:

329   Kolmogorov-Smirnov test, *D=0.108, p=0.1083* and 12-dendrite vs. 3-dendrite: Kolmogorov-

330   Smirnov test, *D=0.040, p=0.9883*). Similarly, pattern separation efficiency was identical

331   across all models and difficulty levels (Figure 8Bii), (12-dendrite vs. 6-dendrite: Wilcoxon

332   test, *W_1=1092.0, p_1=0.2776, 95% CI_1 [-0.04, 0.01], W_2=1106.5, p_2=0.3242, 95% CI_2 [-0.03,*

333   *0.01], W_3=1350.5, p_3=0.4906, 95% CI_3 [-0.01, 0.03], W_4=1378.0, p_4=0.3794, 95% CI_4 [-0.01,*

334   *0.03]* and 12-dendrite vs. 3-dendrite: Wilcoxon test, *W_1=1144.0, p_1=0.4670, 95% CI_1 [-0.03,*

335   *0.01], W_2=937.5, p_2=0.0315, 95% CI_2 [-0.04, 0.00], W_3=1281.0, p_3=0.8335, 95% CI_3 [-0.02,*

336   *0.02], W_4=1117.5, p_4=0.3628, 95% CI_4 [-0.03, 0.01]*). It should be noted that the

337   abovementioned sizes are not realistic for the somata of GC neurons. Nevertheless, these

338   findings highlight the key role of sparsity in controlling pattern separation efficiency,

339   irrespectively of the number of GC dendrites. Moreover, these simulations predict that

340   intrinsic mechanisms of GC neurons could potentially be used to correct for morphological

341   alterations in order to control sparsity levels.

342   We next investigated whether sparsity levels can also be controlled via extrinsic (network)

343   rather than intrinsic mechanisms such as changes in the synaptic weights between EC and

344   GC neurons, namely by decreasing the strength of the input to the DG network. Specifically,

345   the synaptic weight of the EC → GC synapses in the 6- and 3-dendrite models was set to

346   *0.75* and *0.56*, respectively (the control value in the 12-dendrite model was *1.00*). Again, as

347   shown in Figure 8Ci, differences in sparsity were eliminated among the three dendrite

348   models (12-dendrite vs. 6-dendrite: Kolmogorov-Smirnov test, *D=0.092, p = 0.2406* and 12-

349   dendrite vs. 3-dendrite: Kolmogorov-Smirnov test, *D=0.092, p=0.2406*). Finally, pattern

350   separation efficiency was nearly identical cross all models and difficulty levels (Figure 8Cii),

351   with a tiny difference in the 3-dendrite model for patterns overlapping by 90% (12-dendrite

352   vs. 6-dendrite: Wilcoxon test, $W_1=1085.5$, $p_1=0.2582$, 95% CI_1 [-0.04, 0.01], $W_2=1072.5$,

353    $p_2=0.2224$, 95% CI_2 [-0.03, 0.01], $W_3=1316.5$, $p_3=0.6491$, 95% CI_3 [-0.02, 0.02], $W_4=1122.0$,

354    $p_4=0.379495$% CI_4 [-0.03, 0.01] and 12-dendrite vs. 6-dendrite: Wilcoxon test, $W_1=1117.5$,

355    $p_1=0.3628$, 95% CI_1 [-0.04,0.01], $W_2=1052.5$, $p_2=0.1744$, 95% CI_2 [-0.04, 0.01], $W_3=966.0$,

356    $p_3=0.0507$, 95% CI_3 [-0.01, 0.01], $W_4=773.0$, $p_4=0.0010$, 95% CI_4 [-0.05, -0.01)]).

357   In sum, these simulations predict that sparsity is the key determinant of pattern separation

358   efficiency. Sparsity of the GC neuronal population can be controlled via multiple

359   mechanisms, including the growth of dendrites. Pruning of dendrites can be compensated by

360   the growth of very large somata, a large increase in the leak channel conductance or a

361   significant decrease in the strength of the EC input via synaptic weight changes.

362   **What have we learnt from the model?**

363   The above simulations suggest that dendrites contribute to pattern separation via enhancing

364   sparsity, yet they are not essential for this task. Different mechanisms, both intrinsic and

365   extrinsic, can achieve the same effects. What is not entirely clear is whether the relationship

366 between sparsity and pattern separation efficiency is identical for all three GC models across

367 different sparsity levels. To test this we challenged the three models (deduced from the

368 pruning experiment) with the task of separating pairs of inputs that overlap by 80%, while

369 varying the synaptic weight of the EC → GC connections so as to induce different levels of

370 sparsity. Only corrected models (namely exhibiting the same level of sparsity) were

371 compared. As shown in Figure 9A, for any given sparsity level, pattern separation efficiency

372 was almost identical for all three dendrite models (Wilcoxon test, *p>0.05*). These simulations

373 suggest that indeed, when it comes to pattern separation, the key determinant is the level of

374 GC population sparsity. Having multiple dendrites simply helps achieving high levels of

375 sparsity because the probability of generating somatic spikes when inputs are distributed

376 across many (rather than few) dendrites is significantly smaller.

377 Figure 9B summarizes the predictions made by our DG model, whereby sparsity plays a

378 central role in pattern separation. We already knew from previous studies that inhibition is

379 one of the key mechanisms mediating sparsity and in turn pattern separation (Myers and

380 Scharfman, 2009, 2011; Jinde et al., 2012). What we propose here is that the presence of

381 dendrites comes with a bonus in the DG network: it provides another mechanism for

382 increasing sparsity and as such has a key role in pattern separation. While dendrites appear

383 to be sufficient, they are not necessary for achieving high sparsity levels. Both intrinsic and

384 network mechanisms can be used to achieve the same effects. In this study we identified

385 some of these mechanisms but it is likely that there are many others and/or their

386 combinations can also achieve similar results.

Discussion

Summary of the results

The model

The goal of this study was to reveal whether and how dendrites of principal (GC) cells can mediate pattern separation in the DG via the use of a computational approach. Towards this goal, we introduced a novel network model of the DG that includes the four major neuronal cell types found in this area, namely Granule Cells, Mossy Cells, Basket Cells, and HIPP cells. GCs were modeled as two stage integrators via the addition of dendritic branches whose properties are loosely constrained by electrophysiological and anatomical data. The rest of the neuronal types were simulated as exponential leaky integrate-and-fire neurons with adaptation. The proposed hybrid model serves as a bridge between simplified point neuron network models (Myers and Scharfman, 2009) and more detailed biophysical models (Santhakumar et al., 2005) of the DG. As such, it provides a biologically relevant and computationally efficient tool for the in depth exploration of different factors that may contribute to pattern separation, going beyond the scope of this particular study. The selective use of dendritic compartments only in GCs keeps the model complexity low while at the same time allowing the dissection of some basic GC dendritic mechanisms in pattern separation. To our knowledge this is the first DG network model of its kind.

Model predictions

Inhibition is known to control neuronal activity by increasing sparsity, as the number of active neurons is smaller for a given stimulus (Jung and McNaughton, 1993) therefore, enhancing pattern separation (Aimone et al., 2011). In the presented model, inhibition is provided to the network both directly via BCs (perisomatic inhibition) and HIPP cells (dendritic inhibition) and indirectly through the MC circuitry. We find that MC loss, while increasing GC cell activity in

18

411   line with the experimental data of (Ratzliff et al., 2002), does not lead to hyper-excitability yet

412   we do predict a measurable deficit on pattern separation.

413   To our knowledge, our model is the first to predict a role of GC dendrites in pattern

414   separation. This role is an indirect one and results from the inherent increase in sparsity of

415   the GC cells that is endowed by the presence of dendrites. Specifically, we show that the

416   number of GC dendrites correlates positively with pattern separation efficiency due to the

417   higher sparsity levels provided by having multiple dendrites. In our control model, higher

418   sparsity arises from the requirement of having at least two dendrites simultaneously active in

419   order to fire a GC model neuron. This emerged from the calibration of GC properties against

420   experimental data, thus is considered biologically relevant. As a result, GCs with large

421   numbers of dendrites have a lower probability of activation given a fixed number of afferents,

422   therefore increased network sparsity. We also predict that under conditions of dendritic

423   pruning and/or early in the growth stages of GCs, high sparsity can be achieved with

424   alternative mechanisms, both intrinsic (e.g., leak conductance, somatic dimensions) and

425   extrinsic (e.g., synaptic weights) making dendrites a sufficient but not necessary condition for

426   high pattern separation efficiency. These results support the hypothesis that sparsity in GC

427   activity improves pattern separation (O'Reilly and McClelland, 1994) and provide a list of

428   alternative mechanisms for controlling sparsity in the DG.

Implications for pathology

430   As part of the hippocampus, the DG is long hypothesized to play a key role in associative

431   memories, and especially when those are related with events (Morris, 2006). Furthermore,

432   the hippocampal DG has been implicated as the subregion most sensitive to the effects of

433   advancing age (Small et al., 2004). While the CA1 subregion is directly associated with

434   Alzheimer's Disease (AD) due to cell loss, as demonstrated in humans (West et al., 2006),

435   DG alterations have also been reported in patients with the aforementioned disease (Scheff

436   and Price, 2003), including changes in granule cell dendrites (Einstein et al., 1994).

437 Specifically, the dendrites of GCs in AD patients appear shorter, with fewer branches and

438 fewer spines than those of matched controls. Moreover, in AD patients the dendrites of

439 granular cells were reported to lose approximately 50% of their spines (Einstein et al., 1994).

440 Our simulations show that the most important of the above-listed observations with respect

441 to pattern separation performed by the DG would be the shortening of dendritic branches via

442 the loss of branch points rather than the loss of side branches while mentioning the same

443 dendritic length. Total dendritic length of GCs was previously linked to AD, which in turn is

444 aligned with the evidence that patients with AD, who have extensive hippocampal and

445 parahippocampal damage, lost their ability to encode information in distinct, orthogonal

446 representations (Ally et al., 2013).

447 The DG is also associated with epileptogenesis in temporal lobe epilepsy (TLE) and hence,

448 many computational models are used to investigate the effect of GC alterations in epilepsy

449 (Tejada and Roque, 2014; Faghihi and Moustafa, 2015). Moreover, hilar cell loss has been

450 reported in animal models after concussive head injury and also under TLE (Mathern et al.,

451 1995). It remains unclear however, which hilar neurons are lost in animal models of TLE. As

452 a result, there are currently three theories for TLE: a) the "dormant basket cell" hypothesis

453 according to which the hyper-excitability in GC population is due to the loss of MCs which

454 normally excite BCs which in turn provide inhibition to GCs. b) The "irritable mossy cell"

455 hypothesis according to which surviving MCs hyper-excite GCs by sending uncontrolled

456 excitation, and c) the MC loss-induced sprouting hypothesis (mossy fiber sprouting) (Ratzliff

457 et al., 2002). We show that under conditions of MC loss, GCs exhibit increased activity (but

458 not hyper-excitability) which should lead to pattern separation deficits. While our results are

459 in agreement with the findings of (Ratzliff et al., 2002), more experiments need to be

460 performed to revolve this debatable issue.

Simplifications of the model, and future directions

Several simplifications were made in modeling the individual cells and in implementing the DG network. First, we used simple point neurons in order to simulate the neuronal cells of DG. Although these models could capture the average spiking properties of a given neuron, it remains unclear how the geometrical characteristics of those neurons could affect their behavior. Another simplification concerns the effects of synaptic failure rates and receptor desensitization (Harney and Jones, 2002) in the DG, which were not included in the model.

An important aspect of DG function is the long-term synaptic plasticity, by which the connections from PP to GCs are modified. Previous DG models used a form of Hebbian learning that incorporates features of long-term potentiation and depression (Rolls, 2007). However, such a function is most likely to be relevant when stimuli are presented repetitively. On the contrary, the current model is used to distinguish patterns presented in single instances and accordingly, plasticity is not considered. Future work may address such issues along with including other interneuronal populations such as the Molecular layer Perforant Path-associated (MOPP) and the Hilar Commissural-Associational pathway related (HICAP) cells, especially when more data on their intrinsic and connectivity properties become known.

Moreover, GCs are among few cells that undergo neurogenesis in adulthood (Eriksson, 2003; Aimone et al., 2010). In a recent study by Nakashiba et al. (2012), the role of young GCs in pattern separation was investigated and it was concluded that new neurons are required for the discrimination of similar inputs. Since the presented model is used to examine specific alterations of GCs and their effect on pattern separation, neurogenesis is not incorporated but would be considered in the future. Overall, the abovementioned simplifications are unlikely to have a major effect on the basic conclusions about the contribution of morphological alterations of GC dendrites to pattern separation.

Materials and Methods

486

487　The model was developed mainly based on the structure and connectivity features described

488　by Myers and Scharfman (2009), and incorporates the four major dentate cell types. These

489　are the GCs, MCs, BCs and HIPP cells. As the Hilar Commissural-Associational Pathway

490　(HICAP) cells are relatively rare and poorly understood (Sik et al., 1997), they are not

491　included in the model. All simulations were performed using the BRIAN (BRIAN v1.4)

492　network simulator (Goodman and Brette, 2009; Brette and Goodman, 2011) running on a

493　High-Performance Computing Cluster (HPCC) with 312 cores under 64-bit CentOS Linux.

Model neurons

494

495　The four types of DG neurons were modeled as simplified phenomenological neurons of the

496　integrate-and-fire (I&F) type (Izhikevich, 2003; Burkitt, 2006), with no internal geometry

497　("point neurons"). The GCs incorporated dendrites in order to study their role in pattern

498　separation; however the MCs, BCs and HIPP cells were simulated as simple somatic

499　compartments.

500　**Modeling BC, MC and HIPP cells**

501　Specifically, an adaptive exponential I&F model (aEIF) (Brette and Gerstner, 2005) was used

502　to model MCs, BCs and HIPP cells. The model is mathematically described by the following

503　differential equations (Equation 1, 2):

$$C_m \frac{dV_m}{dt} = -g_l(E_l - V_m) + g_l \Delta_T \exp\left(\frac{V_m - V_T}{\Delta_T}\right) + \sum I_{syn} - w \qquad (1)$$

$$\tau_w \frac{dw}{dt} = \alpha(V_m - E_l) - w \qquad (2)$$

504　where C_m is the membrane capacitance, V_m the membrane voltage, g_l the "leak"

505　conductance, E_l the "leak" reversal potential (i.e., the resting potential), I_{syn} the synaptic

506   current flow onto the neuron, w the adaptation variable, Δ_T the slope factor, V_T the effective

507   threshold potential, α the adaptive coupling parameter, and τ_w is the adaptation time

508   constant.

509   The exponential nonlinearity describes the spike action potential and its upswing. In the

510   mathematical interpretation of the model a spike occurs at time t_{spike} when the membrane

511   voltage reaches a finite limit value, and thereafter the downswing of the action potential is

512   described by a reset fixed value V_{reset}, as follows:

513   at $t = t_{spike}\ (V_m \geq V_{threshold})$

$$reset\ V \leftarrow V_{reset},\ w \leftarrow w + b \qquad (3)$$

514   where $V_{threshold}$ is the voltage threshold above which the neuron fires a spike, and b is the

515   spike triggered adaptation parameter. For all neuron types the effective threshold is equal to

516   the voltage threshold (see Table 4 for model parameters).

517   **Modeling principal neurons, GC**

518   In order to investigate the role of GC dendrites in pattern separation, an extended point

519   neuron was implemented. The GC model consisted of a leaky Integrate-and-Fire somatic

520   compartment connected to a variable number of dendritic compartments whose morphology

521   relies on anatomical data (see Table 5 for structure characteristics). Furthermore, an

522   adaptation parameter w was used, only in the somatic compartment, to reproduce spike

523   frequency adaptation reported in these neurons. The equation that describes the membrane,

524   somatic and dendritic, potential of GC model cells is as follows:

$$C_m \frac{dV_m}{dt} = -g_l(E_l - V_m) + \sum I_{syn} - w \qquad (4)$$

23

525   The adaptation parameter (w) was set to zero for the dendritic compartments. There is no

526   evidence for dendritic spikes in GCs (Krueppel et al., 2011), thus the spike mechanism was

527   only applied in the somatic equation.

528   The DG is divided into three distinct layers (Figure 1A), the molecular, granular, and

529   polymorphic (hilus) (Amaral et al., 2007). The GC dendrites extend in the molecular layer

530   (Amaral et al., 2007), which is further divided into the inner, middle, and outer molecular

531   layers, and therefore dendritic compartments are discretized accordingly. Table 5 lists the

532   morphological characteristics of the GC model. According to anatomical data, (Claiborne et

533   al., 1990) GCs have 10-15 dendrites; thus, the control GC model includes 12 dendrites and

534   its physiological responses are validated against experimental data (see Table 4 for GC

535   model parameters).

536   In order to investigate whether the number of GC dendrites affects pattern separation, we

537   used two different approaches; dendritic pruning and growth. First, two more GC models

538   were implemented which differ only in their number of dendrites (6 and 3), but the path

539   length remained the same across these models. Secondly, two GC models were

540   implemented which differ both in their dendritic number and their path length. The

541   morphological differences among the three models are shown in Table 5. The membrane

542   capacitance of the dendritic compartments was increased compared to the somatic one in

543   order to account for spines reported in GC dendrites (Aradi and Holmes, 1999).

544   The intrinsic model properties that were validated against experimental data are the input

545   resistance (R_{in}), the sag ratio, defined as the ratio between the exponentially extrapolated

546   voltage to the steady-state voltage, and the membrane time constant (τ_m). In line with

547   experimental procedures (Lübke et al., 1998), we used 1-second somatic current injection to

548   calculate the intrinsic properties. The input resistance is calculated by the equation $R_{in} =$

549     $\Delta V_m / I_{injected}$, where ΔV_m is the membrane response to current stimulation. Finally, the

550   membrane time-constant is approximated by the formula $\tau_m = R_{in} C_m$, which is a valid

551 approximation for passive compartments. As experimental data were obtained in the

552 presence of synaptic activity blockers, a somatic current injection at the model cell was used

553 to replicate those conditions.

Modeling Synapses

555 Since the DG network consists of both glutamatergic cells (GCs and MCs) and GABAergic

556 interneurons, AMPA, NMDA and GABA synapses were included in the network model.

557 Therefore, the total synaptic current (Equations 1 and 4) consisted of two components; the

558 excitatory current through AMPA receptors (I_{AMPA}) and NMDA receptors (I_{NMDA}), and the

559 inhibitory current via GABA$_\alpha$ receptors (I_{GABA}). The majority of ligand-gated ion channels

560 mediating synaptic transmission, such as AMPA and GABA receptors, display an

561 approximately linear current-voltage relationship when they open. We modeled these

562 channels as an ohmic conductance (g_{syn}) multiplied by the driving force:

$$I_{syn} = g_{syn}(t)\left[V_m(t) - E_{syn}\right] \tag{5}$$

563 where E_{syn} is the AMPA and GABA reversal potential, respectively.

564 The NMDA receptor-mediated conductance depends on the postsynaptic voltage due to the

565 gate blockage by a positively charged magnesium ion (Mg^{2+}). The fraction of NMDA

566 channels that are not blocked by Mg^{2+} can be fitted by a sigmoidal function (Jahr and

567 Stevens, 1990):

$$s(V) = \frac{1}{1 + \eta[Mg^{2+}]_o \exp(-\gamma V_m)} \tag{6}$$

568 where η is the sensitivity of Mg unblock, γ the steepness of Mg unblock, and $[Mg^{2+}]_o$ is the

569 outer magnesium (Mg) concentration. For NMDA receptors in MCs, BCs and HIPP cells we

570 used $\eta = 0.28\,mM^{-1}$, $[Mg^{2+}] = 1mM$, and $\gamma = 0.072\,mV^{-1}$. Instead, for GCs we tuned

571 these parameters in to match the latest experimental data found in literature (Krueppel et al.,

572 2011) with the corresponding values equal to $\eta = 0.2\,\mathrm{mM}^{-1}$, $[\mathrm{Mg}^{2+}] = 2\mathrm{mM}$, and $\gamma =$

573 $0.04\,\mathrm{mV}^{-1}$. Consequently, the NMDA synaptic current is calculated by the following

574 equation:

$$I_{syn} = g_{syn}(t)s(V)\big[V_m(t) - E_{syn}\big] \tag{7}$$

575 The ohmic conductance is simulated as a sum of two exponentials (Bartos et al., 2001), one

576 term based on rising and the other on the decay phase of the postsynaptic potential. This

577 function allows time constants to be set independently. We simulated such a function as a

578 system of linear differential equations (Roth and Van Rossum, 2009):

$$g_{syn}(t) = g_{max}u(t) \tag{8}$$

$$\frac{du}{dt} = -\frac{u}{\tau_{decay}} + h_0 v(1-u), \frac{dv}{dt} = -\frac{v}{\tau_{rise}} \tag{9}$$

579 where τ_{rise} and τ_{decay} are the rise and decay constants respectively, h_0 a scaling factor and

580 $u(t)$ is the function of two exponentials $u(t) = \exp(-t/\tau_{decay}) - \exp(-t/\tau_{rise})$, which is

581 divided by its maximum amplitude. The scaling factor is set to $1\,\mathrm{ms}^{-1}$ for all AMPA and

582 GABA receptors and all neuronal types. The NMDA scaling factor is set to $0.5\,\mathrm{ms}^{-1}$ apart

583 from the synapses form on GCs where it is set to $2\,\mathrm{ms}^{-1}$. Because axons of neurons are not

584 included in the model, a delay is used between pre- and postsynaptic transmission. The role

585 of the delay is to account for both the synaptic transmission and the axonal conduction

586 delay, and its value depends on the presynaptic and postsynaptic neuronal types. The peak

587 conductance (g_{max}), rise and decay time constants, and the delay of various network

588 connections were estimated from experimental data (Kneisler and Dingledine, 1995; Geiger

589 et al., 1997; Bartos et al., 2001; Schmidt-Hieber et al., 2007; Larimer and Strowbridge, 2008;

590 Schmidt-Hieber and Bischofberger, 2010; Krueppel et al., 2011; Chiang et al., 2012) and are

591 given in Table 6. Specifically, the GC peak conductance both for AMPA and NMDA, was

592 validated against experimental data (Krueppel et al., 2011), where it is evidenced that a

593   single synapse provokes a $0.6\,\mathrm{mV}$ somatic EPSP, and also the NMDA and AMPA peak

594   current ratio is equal to 1.08. These values were reproduced in the GC model cells. The

595   models also incorporate background activity, in order to simulate the experimental findings of

596   spontaneous activity in DG. Accordingly, we used Poisson independent spike trains in order

597   to reproduce the experimental data for MCs (2-4 Hz spontaneous activity) (Henze and

598   Buzsáki, 2007) and for BCs (1-2 Hz spontaneous activity) (Kneisler and Dingledine, 1995).

599   GCs infrequently generate spontaneously activity, even if inhibition is blocked (Lynch et al.,

600   2000). Thus, we implemented noisy inputs in order to only evoke spontaneous EPSPs (0.05

601   Hz spontaneous activity).

The DG network model

603   The DG network model consists of 2000 simulated GCs, a scale that represents 1/500 of the

604   one million GCs found in rat brains (West et al., 1991). The chosen number of GCs provides

605   enough power to explore pattern separation, while maintaining computational efficiency. The

606   population of GCs is organized in non-overlapping clusters, with each cluster containing 20

607   GCs, respectively. This kind of organization roughly corresponds to the lamellar organization

608   along the septotemporal extent of DG (Sloviter and Lømo, 2012).

609   Apart from the principal excitatory dentate cells (GCs), the model comprises two kind of

610   inhibitory interneurons, the perisomatic (BCs), which form synapses at the soma of the GCs,

611   and dendritic (HIPP) inhibitory cells, which contact the GCs at their distal dendritic

612   compartments. There is one BC per cluster of GCs, which in turn corresponds to 100

613   simulated BCs in the model. This is a form of "winner-take-all" competition (Coultrip et al.,

614   1992) in which all, but the most strongly activated GCs in a cluster, are silenced. Given 100

615   clusters in the model, and with one winner within each cluster, approximately 5% of GCs are

616   active for a given stimulus; this is in agreement with the theoretically and experimentally

617   estimation of 2-5% granular activity in the substrate (Treves et al., 2008; Danielson et al.,

618   2016). Moreover, the model includes simulated hilar MCs and HIPP cells. Estimated

619   numbers for these neuronal types vary from 30,000 to 50,000 MCs in rats (West et al., 1991;

620   Buckmaster and Jongen-Rêlo, 1999), which in turn corresponds to 3-5 MCs per 100 GCs.

621   Accordingly, the model includes 80 MCs per 2,000 GCs. Experimental counts for HIPP cells

622   vary significantly, but the latest estimates suggest about 12,000 HIPP cells in rats

623   (Buckmaster and Jongen-Rêlo, 1999) meaning less than 2 HIPP cells per 100 GCs. To

624   reflect this empirical data, we simulated 40 HIPP cells in the network model (Figure 1A).

625   External input to the network model is provided by 400 afferents representing the major input

626   that DG receives from Entorhinal Cortex (EC) Layer II cells, via the Perforant Path (PP). The

627   ratio of GCs to PP afferents is aligned with estimations of about 200,000 EC Layer II cells in

628   the rat (Amaral et al., 1990), suggesting a ratio of 20 EC cells per 100 GCs. Therefore, the

629   model incorporates synaptic input that corresponds to 400 EC Layer II cells. For simplicity,

630   the input cells are simulated as independent Poisson spike trains, with frequency of 40 Hz,

631   which is in line with experimental data (Hafting et al., 2005). Previous experimental studies

632   have shown that dentate GCs receive input from 10% of the 4,000 afferents that contact a

633   given GC in the rat during a task (McNaughton et al., 1991), which in turn suggests that an

634   approximate 10% of EC Layer II cells are active. The simulations reported here assume that

635   10% is the active PP afferents representing a given stimulus. According to McNaughton et

636   al., 1991, 10% of the total entorhinal input is necessary to discharge one GC. However, the

637   EC-GC connection is sparse, with each GC receiving input from about 2% of EC Layer II

638   neurons. Assuming only 400 input cells; one GC could have only 8 afferents from EC, which

639   in turn would make it impossible for the GC to become active. As a compromise, we used a

640   randomly determined 20% of EC Layer II cells as input to each GC and additionally, 20%

641   randomly determined EC Layer II cells as input to each HIPP cell; GCs contact each MC

642   with 20% probability; GCs and HIPP cells each feedback to contact a randomly determined

643   20% of GCs and finally, each MC connects with every BC in the network. Connections are

644   initialized randomly (uniform random distribution) before the start of the simulations and

645   remain fixed across all simulations (no rewiring). The connectivity matrix was the same for all

28

646   experiments and across all using GC models, apart from the PP→GC, and HIPP→GC

647   synapses due to the difference in GC number of dendrites.

Pattern Separation and Data Analysis

649   Generally, a network performs pattern separation whenever the similarity between two

650   distinct input patterns is higher than the similarity between the corresponding output patterns

651   (Figure 1B). In this work, the input patterns are presented as the activity along the 400 PP

652   afferents. Each input pattern has 40 active PP afferents (10% input density), an amount of

653   which are common between two patterns; hence the two patterns have a degree of

654   similarity. Active cell is considered every GC that fires at least one spike during stimulus

655   presentation (Myers and Scharfman, 2009), thus the output patterns correspond to the active

656   GCs. In order to quantify the pattern separation efficiency we used a metric denoted by f_1

657   ('population distance'):

$$f_{1(i,o)} = \frac{\mathrm{HD}_{i,o}}{2(1 - s_{i,o})\mathrm{N}_{i,o}} \tag{10}$$

658   where the i and o subscripts denote input and output, respectively, s denotes the sparsity

659   (i.e., the ratio of silent neurons to all neurons), N the number of neurons, and HD is the

660   hamming distance between two binary patterns (Hamming, 1950), defined as the number of

661   positions at which the corresponding values are different. The factor of 2 in the denominator

662   is used to limit our distance measure at zero. Our network is said to perform pattern

663   separation if the input distance is smaller than the output distance, i.e., when $f_{1(i)} < f_{1(o)}$.

664   Thus far, the distance between two binary patterns is calculated using only the HD metric.

665   Although we construct the input patterns to have the same sparsity (i.e., 10% are active), the

666   corresponding output patterns do not necessarily have the same activity level. As we want to

667   examine the differences among the active neurons of each pattern we disengage the

668   dependence on sparsity by dividing the HD with the number of neurons that are active in a

669   pattern. In our case, the output patterns are vectors, each with length equal to 2000 and 2-

670 5% active neurons in 12 dendrites case, which in turn correspond to 40-100 neurons. The

671 total number of active neurons lies in the range of 40-200. For example, if the HD between

672 two patterns is 20, the old metric gives a distance equal to 0.01 whereas the f_1 metric

673 ranges from 0.10-0.25, depending on the percentage of active GC neurons. Thus, using the

674 proposed f_1 metric, differences only between active neurons are taken into account, making

675 the metric more robust across different levels of sparsity.

676 We constructed four groups of input pattern pairs, with different degrees of similarity and

677 calculated the input and the corresponding output population distances for each group

678 independently. Firstly, we constructed a variety of input patterns with input density 10% (i.e.,

679 40 active neurons) and consequently, four additional input patterns were built with 40 active

680 neurons, 8, 16, 24 and 32 of which are common between patterns, respectively, which, in

681 turn, corresponds to $f_{1(input)} = 0.4, 0.3, 0.2$ and 0.1. The reasoning behind this approach is to

682 examine highly overlapping patterns $(f_{1(input)} = 0.1, 0.2)$, as well as less similar ones

683 $(f_{1(input)} = 0.3, 0.4)$. Thus, each trial was composed of two simulations using two input

684 patterns within each group.

685 Whereas the f_1 metric quantifies the distance between two binary vectors containing active

686 and non-active neurons ('population distance'), we used an additional metric, denoted by f_2,

687 which quantifies the distance in the firing rates of common neurons that encode two patterns

688 by using their firing rates ('rate distance') (Figure 1C). The f_2 metric is calculated by dividing,

689 for each neuron that is active in both patterns, its mean firing rate given one stimulus (40 Hz)

690 by its mean firing rate given a stronger stimulus (50 Hz), and averaging these ratios across

691 the population of input and output neurons, respectively (Leutgeb et al., 2004). We subtract

692 this ratio from one in order to convert the 'rate similarity' into a 'rate distance':

$$f_2 = 1 - \frac{1}{N_c} \sum_{j=1}^{N_c} \frac{\left(r_{B,j} - \min r_B\right)}{\left(r_{A,j} - \min r_A\right)} \tag{11}$$

693   where N_c denotes the number of common neurons that are active for bot inputs, r the firing

694   rate of *j-th* neuron using input A and B, respectively. Here, B represents the low firing

695   frequency input, while A the high frequency input. We subtract the global minimum firing rate

696   of GCs found in all trials in order to normalize the dynamic range of firing rates.

697   For this experiment, the population of active EC neurons in each pair of inputs was identical.

698   The network performs pattern separation if the input 'rate distance' is smaller than the

699   corresponding distance in the output, i.e., $f_{2(input)} < f_{2(output)}$. In each trial, the two stimuli

700   were presented to the network and their 'rate distance', both in input and output, was

701   estimated. The results were then averaged across all trials (50 trials for each model).

702   For each trial, the network was simulated for *850* milliseconds (ms). The first *300* ms were

703   simulated in order for the network to reach its stable state, so they were excluded from the

704   analysis. The input onset was at *300* ms and the stimulus was applied for *500* ms. The last

705   *50* ms were simulated in order for the network to reach again its steady state and they were

706   excluded from the analysis as well. The time step for all simulations was set to *0.1* ms.

707   The data analysis and the figures describing the results were made using custom made

708   programs in python2.7.10™ (www.python.org) while the statistical analysis was made using

709   the R3.3.1 programming language (https://www.r-project.org). We used the two-sided, two-

710   sample Wilcoxon signed-rank test for the pattern separation efficiency comparison and the

711   two-sided, two-sample Kolmogorov-Smirnov test (K-S test) to compare the GC activity

712   probability density functions (Neuhäuser, 2011). The model will be available for download at

713   http://dendrites.gr/en/publications-8/software-23.

714

Acknowledgements

715

716   We would like to thank Alessandro Treves, Idan Segev and Nelson Spruston for their

717   valuable feedback on the project. In addition, we would like to thank Athanasia Papoutsi and

718   Panagiotis Bozelos for their helpful comments on the manuscript, as well as George

719   Kastellakis for his assistance in the software implementation and Pavlos Pavlidis for his

720   guidance on the statistical analysis and finally, all members of the Poirazi lab for their

721   comments during the various phases of the project.

Competing interests

722

723   The authors declare that no competing interests exist.

References

724

725 Aimone JB, Deng W, Gage FH. (2010). Adult neurogenesis: Integrating theories and

726 separating functions. *Trends Cogn Sci* **14**:325–337. doi:

727 http://dx.doi.org/10.1016/j.tics.2010.04.003

728 Aimone JB, Deng W, Gage FH. (2011). Resolving New Memories: A Critical Look at the

729 Dentate Gyrus, Adult Neurogenesis, and Pattern Separation. *Neuron* **70**:589–596. doi:

730 http://dx.doi.org/10.1016/j.neuron.2011.05.010

731 Ally BA, Hussey EP, Ko PC, Molitor RJ. (2013). Pattern separation and pattern completion in

732 Alzheimer's disease: Evidence of rapid forgetting in amnestic mild cognitive impairment.

733 *Hippocampus* **23**:1246–1258. doi: http://doi.wiley.com/10.1002/hipo.22162

734 Amaral DG, Ishizuka N, Claiborne B. (1990). Neurons, numbers and the hippocampal

735 network. *Prog Brain Res* **83**:1–11. doi: http://www.ncbi.nlm.nih.gov/pubmed/2203093

736 Amaral DG, Scharfman HE, Lavenex P. (2007). The dentate gyrus: fundamental

737 neuroanatomical organization (dentate gyrus for dummies). In: The Dentate Gyrus: A

738 comprehensive guide to structure, function, and clinical implications (Scharfman HE, ed),

739 pp 3–22. Amsterdam: Elsevier B.V.

740 Aradi I, Holmes WR. (1999). Role of multiple calcium and calcium-dependent conductances

741 in regulation of hippocampal dentate granule cell excitability. *J Comput Neurosci* **6**:215–

742 235.

743 Bakker A, Kirwan CB, Miller M, Stark CEL. (2008). Pattern separation in the human

744 hippocampal CA3 and dentate gyrus. *Science* **319**:1640–1642.

745 Bartos M, Vida I, Frotscher M, Geiger JR, Jonas P. (2001). Rapid signaling at inhibitory

746 synapses in a dentate gyrus interneuron network. *J Neurosci* **21**:2687–2698. doi:

747 http://www.ncbi.nlm.nih.gov/pubmed/11306622

748 Bolz L, Heigele S, Bischofberger J. (2015). Running Improves Pattern Separation during

749   Novel Object Recognition. **1**:129–141.

750   Brette R, Gerstner W. (2005). Adaptive Exponential Integrate-and-Fire Model as an Effective

751   Description of Neuronal Activity. *J Neurophysiol* **94**:3637–3642. doi:

752   http://jn.physiology.org/cgi/doi/10.1152/jn.00686.2005

753   Brette R, Goodman DFM. (2011). Vectorized algorithms for spiking neural network

754   simulation. *Neural Comput* **23**:1503–1535. doi:

755   http://www.mitpressjournals.org/doi/abs/10.1162/NECO_a_00123

756   Buckmaster PS, Jongen-Rêlo AL. (1999). Highly specific neuron loss preserves lateral

757   inhibitory circuits in the dentate gyrus of kainate-induced epileptic rats. *J Neurosci*

758   **19**:9519–9529.

759   Burkitt AN. (2006). A Review of the Integrate-and-fire Neuron Model: I. Homogeneous

760   Synaptic Input. *Biol Cybern* **95**:1–19. doi: http://link.springer.com/10.1007/s00422-006-

761   0068-6

762   Chiang PH, Wu PY, Kuo TW, Liu YC, Chan CF, Chien TC, Cheng JK, Huang YY, Chiu C Di,

763   Lien CC. (2012). GABA Is Depolarizing in Hippocampal Dentate Granule Cells of the

764   Adolescent and Adult Rats. *J Neurosci* **32**:62–67.

765   Claiborne BJ, Amaral DG, Cowan WM. (1990). Quantitative, three-dimensional analysis of

766   granule cell dendrites in the rat dentate gyrus. *J Comp Neurol* **302**:206–219.

767   Coultrip R, Granger R, Lynch G. (1992). A cortical model of winner-take-all competition via

768   lateral inhibition. *Neural Networks* **5**:47–54.

769   Danielson NB, Kaifosh P, Zaremba JD, Lovett-Barron M, Tsai J, Denny CA, Balough EM,

770   Goldberg AR, Drew LJ, Hen R, Losonczy A, Kheirbek MA. (2016). Distinct Contribution of

771   Adult-Born Hippocampal Granule Cells to Context Encoding. *Neuron* **90**:101–112.

772   Das T, Ivleva EI, Wagner AD, Stark CEL, Tamminga CA. (2014). Loss of pattern separation

773   performance in schizophrenia suggests dentate gyrus dysfunction. *Schizophr Res*

774   **159**:193–197. doi: http://linkinghub.elsevier.com/retrieve/pii/S0920996414002357

775 Deng W, Aimone JB, Gage FH. (2010). New neurons and new memories: how does adult

776   hippocampal neurogenesis affect learning and memory? *Nat Rev Neurosci* **11**:339–350.

777   doi: http://dx.doi.org/10.1038/nrn2822

778 Einstein G, Buranosky R, Crain BJ. (1994). Dendritic pathology of granule cells in

779   Alzheimer's disease is unrelated to neuritic plaques. *J Neurosci* **14**:5077–5088.

780 Engin E, Zarnowska ED, Benke D, Tsvetkov E, Sigal M, Keist R, Bolshakov VY, Pearce RA,

781   Rudolph U. (2015). Tonic Inhibitory Control of Dentate Gyrus Granule Cells by 5-

782   Containing GABAA Receptors Reduces Memory Interference. *J Neurosci* **35**:13698–

783   13712. doi: http://www.jneurosci.org/cgi/doi/10.1523/JNEUROSCI.1370-15.2015

784 Erevitt BS, Skrondal A. (2010). The Cambridge dictionary of Statistics, 4th ed. Cambridge:

785   Cambridge University Press.

786 Eriksson PS. (2003). Neurogenesis and its implications for regeneration in the adult brain. *J*

787   *Rehabil Med* **35**:17–19.

788 Faghihi F, Moustafa AA. (2015). A computational model of pattern separation efficiency in

789   the dentate gyrus with implications in schizophrenia. *Front Syst Neurosci* **09**:1–12. doi:

790   http://journal.frontiersin.org/article/10.3389/fnsys.2015.00042

791 Geiger JRP, Lübke J, Roth A, Frotscher M, Jonas P. (1997). Submillisecond AMPA receptor-

792   mediated signaling at a principal neuron- interneuron synapse. *Neuron* **18**:1009–1023.

793 Goodman DFM, Brette R. (2009). The Brian simulator. *Front Neurosci* **3**:192–197. doi:

794   http://journal.frontiersin.org/article/10.3389/neuro.01.026.2009/abstract

795 Hafting T, Fyhn M, Molden S, Moser MB, Moser EI. (2005). Microstructure of a spatial map

796   in the entorhinal cortex. *Nature* **436**:801–806.

797 Hamming RW. (1950). Error Detecting and Error Correcting Codes. *Bell Syst Tech J*

798   **29**:147–160.

799 Harney SC, Jones M V. (2002). Pre- and postsynaptic properties of somatic and dendritic

800   inhibition in dentate gyrus. *Neuropharmacology* **43**:584–594.

801   Henze DA, Buzsáki G. (2007). Hilar mossy cells: functional identification and activity in vivo.

802   In: The Dentate Gyrus: A comprehensive guide to structure, function, and clinical

803   implications (Scharfman HE, ed), pp 199–216. Amsterdam: Elsevier B.V. doi:

804   http://linkinghub.elsevier.com/retrieve/pii/S007961230763012X

805   Ikrar T, Guo N, He K, Besnard A, Levinson S, Hill A, Lee HK, Hen R, Xu X, Sahay A. (2013).

806   Adult neurogenesis modifies excitability of the dentate gyrus. *Front Neural Circuits* **7**:204.

807   doi:

808   http://www.pubmedcentral.nih.gov/articlerender.fcgi?artid=3872742&tool=pmcentrez&ren

809   dertype=abstract

810   Izhikevich EM. (2003). Simple model of spiking neurons. *IEEE Trans Neural Netw* **14**:1569–

811   1572. doi: http://www.ncbi.nlm.nih.gov/pubmed/18244602

812   Jahr CE, Stevens CF. (1990). Voltage dependence of NMDA-activated macroscopic

813   conductances predicted by single-channel kinetics. *J Neurosci* **10**:3178–3182.

814   Jain S, Yoon SY, Zhu L, Brodbeck J, Dai J, Walker D, Huang Y. (2012). Arf4 Determines

815   Dentate Gyrus-Mediated Pattern Separation by Regulating Dendritic Spine Development.

816   *PLoS One* **7**:1–15.

817   Jinde S, Zsiros V, Jiang Z, Nakao K, Pickel J, Kohno K, Belforte JE, Nakazawa K. (2012).

818   Hilar Mossy Cell Degeneration Causes Transient Dentate Granule Cell Hyperexcitability

819   and Impaired Pattern Separation. *Neuron* **76**:1189–1200. doi:

820   http://dx.doi.org/10.1016/j.neuron.2012.10.036

821   Jinde S, Zsiros V, Nakazawa K. (2013). Hilar mossy cell circuitry controlling dentate granule

822   cell excitability. *Front Neural Circuits* **7**:14. doi:

823   http://www.pubmedcentral.nih.gov/articlerender.fcgi?artid=3569840&tool=pmcentrez&ren

824   dertype=abstract

825   Johnston ST, Shtrahman M, Parylak S, Gonçalves JT, Gage FH. (2015). Paradox of Pattern

826   Separation and Adult Neurogenesis: A Dual Role for New Neurons Balancing Memory

827   Resolution and Robustness. *Neurobiol Learn Mem* doi:

828   http://linkinghub.elsevier.com/retrieve/pii/S1074742715001938

829   Jung MW, McNaughton BL. (1993). Spatial selectivity of unit activity in the hippocampal

830   granular layer. *Hippocampus* **3**:165–182.

831   Kirwan CB, Stark CEL. (2007). Overcoming interference: an fMRI investigation of pattern

832   separation in the medial temporal lobe. *Learn Mem* **14**:625–633.

833   Kneisler TB, Dingledine R. (1995). Spontaneous and synaptic input from granule cells and

834   the perforant path to dentate basket cells in the rat hippocampus. *Hippocampus* **5**:151–

835   164.

836   Krueppel R, Remy S, Beck H. (2011). Dendritic integration in hippocampal dentate granule

837   cells. *Neuron* **71**:512–528. doi: http://dx.doi.org/10.1016/j.neuron.2011.05.043

838   Lacy JW, Yassa MA, Stark SM, Muftuler LT, Stark CEL. (2011). Distinct pattern separation

839   related transfer functions in human CA3/dentate and CA1 revealed using high-resolution

840   fMRI and variable mnemonic similarity. *Learn Mem* **18**:15–18.

841   Larimer P, Strowbridge BW. (2008). Nonrandom local circuits in the dentate gyrus. *J*

842   *Neurosci* **28**:12212–12223.

843   Leutgeb JK, Leutgeb S, Moser MB, Moser EI. (2007). Pattern separation in the dentate

844   gyrus and CA3 of the hippocampus. *Science* **315**:961–966.

845   Leutgeb JK, Leutgeb S, Treves A, Meyer R, Barnes CA, McNaughton BL, Moser MB, Moser

846   EI. (2005). Progressive transformation of hippocampal neuronal representations in

847   "morphed" environments. *Neuron* **48**:345–348.

848   Leutgeb S, Leutgeb JK, Treves A, Moser MB, Moser EI. (2004). Distinct Ensemble Codes in

849   Hippocampal Areas CA3 and CA1. *Science (80-)* **305**:1295–1298. doi:

850   http://www.sciencemag.org/cgi/doi/10.1126/science.1100265

851   Lübke J, Frotscher M, Spruston N. (1998). Specialized electrophysiological properties of

852   anatomically identified neurons in the hilar region of the rat fascia dentata. *J Neurophysiol*

853   **79**:1518–1534.

854   Lynch M, Sayin U, Golarai G, Sutula T. (2000). NMDA receptor-dependent plasticity of

855   granule cell spiking in the dentate gyrus of normal and epileptic rats. *J Neurophysiol*

856   **84**:2868–2879.

857   Marr D. (1971). Simple Memory : A Theory for Archicortex. *Philos Trans R Soc Lond B Biol*

858   *Sci* **262**:23–81.

859   Marrone DF, Adams AA, Satvat E. (2011). Increased pattern separation in the aged fascia

860   dentata. *Neurobiol Aging* **32**:2317.e23–e32. doi:

861   http://dx.doi.org/10.1016/j.neurobiolaging.2010.03.021

862   Mathern GW, Babb TL, Vickrey BG, Melendez M, Pretorius JK. (1995). The clinical-

863   pathogenic mechanisms of hippocampal neuron loss and surgical outcomes in temporal

864   lobe epilepsy. *Brain* **118**:105–118. doi:

865   http://www.brain.oxfordjournals.org/lookup/doi/10.1093/brain/118.1.105

866   McNaughton BL, Barnes CA, Mizumori SJY, Green EJ, Sharp PE. (1991). Contribution of

867   granule cells to spatial representations in hippocampal circuits: a puzzle. In: Kindling and

868   Synaptic Plasticity: The Legacy of Graham Goddar (Morrell F, ed), pp 110–123. Boston:

869   Springer-Verlag.

870   Morris RGM. (2006). Elements of a neurobiological theory of hippocampal function: the role

871   of synaptic plasticity, synaptic tagging and schemas. *Eur J Neurosci* **23**:2829–2846. doi:

872   http://doi.wiley.com/10.1111/j.1460-9568.2006.04888.x

873   Motley SE, Kirwan CB. (2012). A Parametric Investigation of Pattern Separation Processes

874   in the Medial Temporal Lobe. *J Neurosci* **32**:13076–13084.

875   Myers CE, Scharfman HE. (2009). A Role for hilar cells in pattern separation in the dentate

876   gyrus: A computational approach. *Hippocampus* **19**:321–337.

877 Myers CE, Scharfman HE. (2011). Pattern separation in the dentate gyrus: A role for the

878   CA3 backprojection. *Hippocampus* **21**:1190–1215.

879 Nakashiba T, Cushman JD, Pelkey KA, Renaudineau S, Buhl DL, McHugh TJ, Barrera VR,

880   Chittajallu R, Iwamoto KS, McBain CJ, Fanselow MS, Tonegawa S. (2012). Young

881   dentate granule cells mediate pattern separation, whereas old granule cells facilitate

882   pattern completion. *Cell* **149**:188–201. doi: http://dx.doi.org/10.1016/j.cell.2012.01.046

883 Neuhäuser M. (2011). Nonparametric Statistical Tests: A Computational Approach. New

884   York: CRC Press. doi: papers3://publication/uuid/1A2A31AE-B983-4060-BD27-

885   C5B73222FF1C

886 Nitz D, McNaughton B. (2004). Differential modulation of CA1 and dentate gyrus

887   interneurons during exploration of novel environments. *J Neurophysiol* **91**:863–872.

888 O'Reilly RC, McClelland JL. (1994). Hippocampal Conjunctive Encoding, Storage, and

889   Recall: Avoiding a Trade-Off. *Hippocampus* **4**:661–682. doi:

890   http://www.ncbi.nlm.nih.gov/pubmed/7704110

891 Olshausen BA, Field DJ. (2004). Sparse coding of sensory inputs. *Curr Opin Neurobiol*

892   **14**:481–487.

893 Petrantonakis PC, Poirazi P. (2014). A compressed sensing perspective of hippocampal

894   function. *Front Syst Neurosci* **8**:1–13. doi:

895   http://journal.frontiersin.org/Journal/10.3389/fnsys.2014.00141/abstract

896 Petrantonakis PC, Poirazi P. (2015). Dentate Gyrus Circuitry Features Improve Performance

897   of Sparse Approximation Algorithms Dehghani F, ed. *PLoS One* **10**:e0117023. doi:

898   http://dx.plos.org/10.1371/journal.pone.0117023

899 Ratzliff ADH, Howard AL, Santhakumar V, Osapay I, Soltesz I. (2004). Rapid deletion of

900   mossy cells does not result in a hyperexcitable dentate gyrus: implications for

901   epileptogenesis. *J Neurosci* **24**:2259–2269.

902 Ratzliff AH, Santhakumar V, Howard A, Soltesz I. (2002). Mossy cells in epilepsy: Rigor

903   mortis or vigor mortis? *Trends Neurosci* **25**:140–144.

904   Rolls ET. (2007). An attractor network in the hippocampus: theory and neurophysiology.

905   *Learn Mem* **14**:714–731.

906   Roth A, Van Rossum MCW. (2009). Modeling synapses. In: Computational modeling

907   methods for neuroscientists (De Shutter E, ed), pp 139–160. Cambridge, MA: MIT press.

908   Santhakumar V, Aradi I, Soltesz I. (2005). Role of mossy fiber sprouting and mossy cell loss

909   in hyperexcitability: a network model of the dentate gyrus incorporating cell types and

910   axonal topography. *J Neurophysiol* **93**:437–453.

911   Santoro A. (2013). Reassessing pattern separation in the dentate gyrus. *Front Behav*

912   *Neurosci* **7**:1–4. doi:

913   http://journal.frontiersin.org/article/10.3389/fnbeh.2013.00096/abstract

914   Satvat E, Schmidt B, Argraves M, Marrone DF, Markus EJ. (2011). Changes in task

915   demands alter the pattern of zif268 expression in the dentate gyrus. *J Neurosci* **31**:7163–

916   7167.

917   Scheff SW, Price DA. (2003). Synaptic pathology in Alzheimer's disease: A review of

918   ultrastructural studies. *Neurobiol Aging* **24**:1029–1046.

919   Schmidt-Hieber C, Bischofberger J. (2010). Fast sodium channel gating supports localized

920   and efficient axonal action potential initiation. *J Neurosci* **30**:10233–10242.

921   Schmidt-Hieber C, Jonas P, Bischofberger J. (2007). Subthreshold dendritic signal

922   processing and coincidence detection in dentate gyrus granule cells. *J Neurosci* **27**:8430–

923   8441.

924   Sik A, Penttonen M, Buzsaki G. (1997). Interneurons in the Hippocampal Dentate Gyrus : an

925   In Vivo Intracellular Study. *Eur J Neurosci* **9**:573–588.

926   Sloviter RS, Lømo T. (2012). Updating the lamellar hypothesis of hippocampal organization.

927   *Front Neural Circuits* **6**:102. doi:

928   http://www.pubmedcentral.nih.gov/articlerender.fcgi?artid=3517983&tool=pmcentrez&ren

929   dertype=abstract

930 Small SA, Chawla MK, Buonocore M, Rapp PR, Barnes CA. (2004). Imaging correlates of

931   brain function in monkeys and rats isolates a hippocampal subregion differentially

932   vulnerable to aging. *Proc Natl Acad Sci U S A* **101**:7181–7186.

933 Squire LR, Stark CEL, Clark RE. (2004). The medial temporal lobe. *Annu Rev Neurosci*

934   **27**:279–306.

935 Tejada J, Roque AC. (2014). Computational models of dentate gyrus with epilepsy-induced

936   morphological alterations in granule cells. *Epilepsy Behav* **38**:63–70. doi:

937   http://dx.doi.org/10.1016/j.yebeh.2014.02.007

938 Treves A, Rolls ET. (1994). Computational Analysis of the Role of the Hippocampus in

939   Memory. *Hippocampus* **4**:374–391.

940 Treves A, Tashiro A, Witter MP, Moser EI. (2008). What is the mammalian dentate gyrus

941   good for? *Neuroscience* **154**:1155–1172. doi:

942   http://linkinghub.elsevier.com/retrieve/pii/S0306452208006660

943 West MJ, Kawas CH, Martin LJ, Troncoso JC. (2006). The CA1 Region of the Human

944   Hippocampus Is a Hot Spot in Alzheimer's Disease. *Ann N Y Acad Sci* **908**:255–259. doi:

945   http://doi.wiley.com/10.1111/j.1749-6632.2000.tb06652.x

946 West MJ, Slomianka L, Gundersen HJ. (1991). Unbiased stereological estimation of the total

947   number of neurons in thesubdivisions of the rat hippocampus using the optical

948   fractionator. *Anat Rec* **231**:482–497.

949 Yassa MA, Stark CEL. (2011). Pattern separation in the hippocampus. *Trends Neurosci*

950   **34**:515–525. doi: http://dx.doi.org/10.1016/j.tins.2011.06.006

951 Yim MY, Hanuschkin A, Wolfart J. (2015). Intrinsic rescaling of granule cells restores pattern

952   separation ability of a dentate gyrus network model during epileptic hyperexcitability.
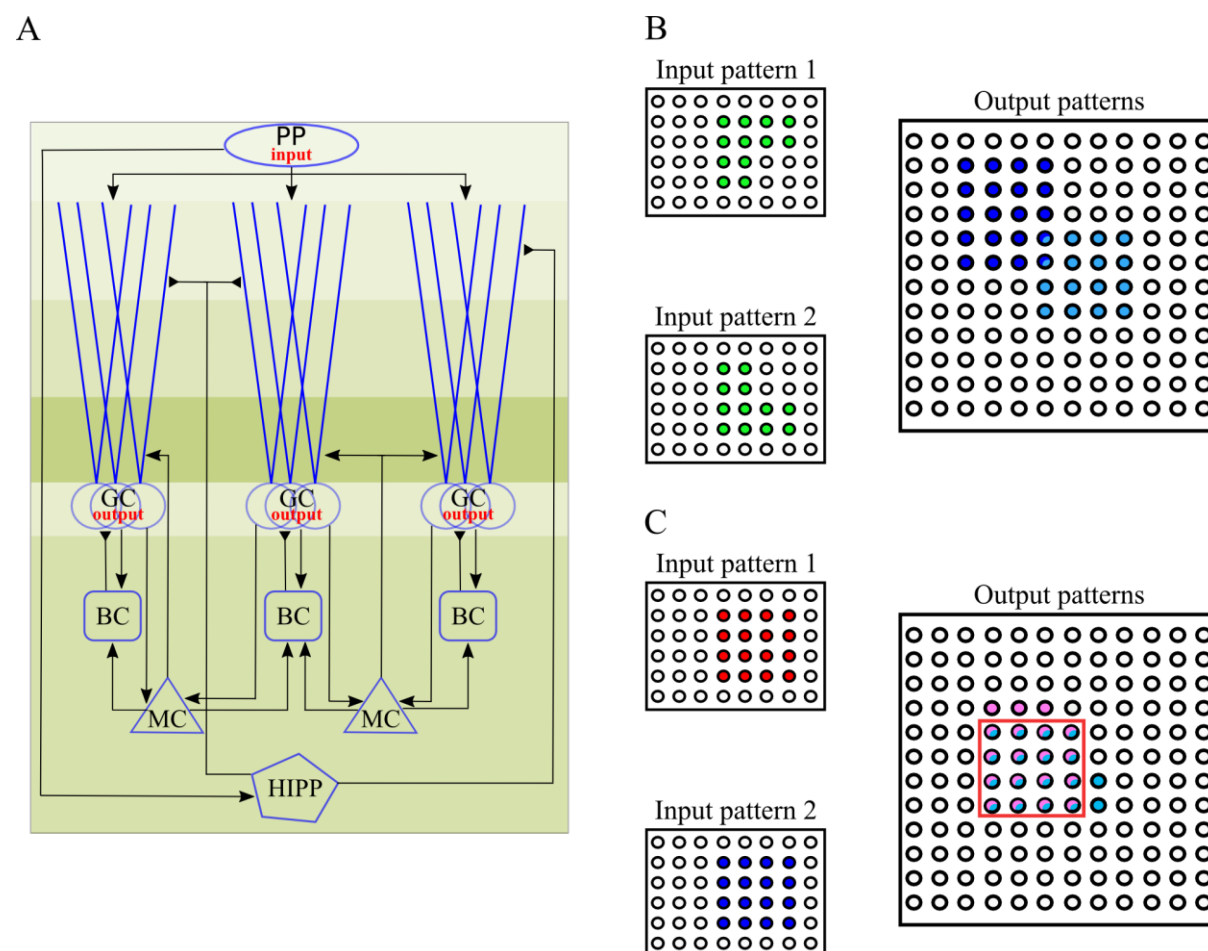
953   *Hippocampus* **25**:297–308. doi: http://doi.wiley.com/10.1002/hipo.22373

954 # Figures

955

956 **Figure 1. A.** Schematic representation of the implemented DG network model. Different shades of green

957 illustrate the layer division. PP: Perforant Path, GC: Granule Cells, BC: Basket Cells, MC: Mossy Cells, HIPP:

958 Hilar Perforant Path-associated cells. Perforant Path afferents curry the input to the network, and project on both

959 the GCs and the HIPP cells. MCs and GCs are connected in a recurrent manner. MCs also excite the BCs.

960 Inhibition of GCs is provided through BCs and HIPP cells directly and indirectly via MCs. Note that HIPP cells

961 contact the distal dendrites rather than the soma of GCs. GCs provide the output of the DG network. **B.**

962 Schematic representation of pattern separation using population-based coding. When two highly overlapping EC

963 inputs (input 1 & 2, with identical mean firing rates) arrive in DG, the corresponding outputs are highly dissimilar.

964 Note that the output pattern is sparse because of the low number of GCs that encode any given pattern. **C.**

965 Schematic representation of pattern separation using rate-based coding. When two highly overlapping EC inputs

966 (input 1 & 2, with different mean firing rates but identical input populations) arrive in DG, the corresponding

967 outputs are highly dissimilar in their firing rates but also likely to differ in the populations they activate. Rate

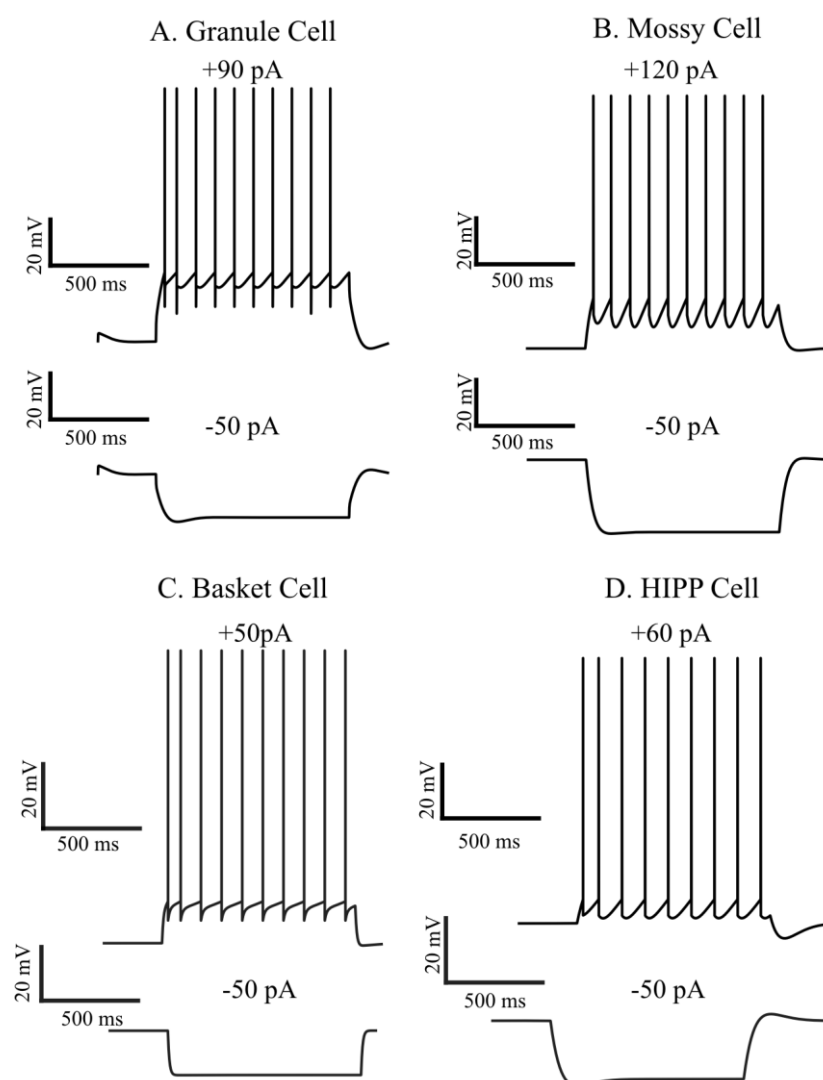968 distances are estimated over the set of common neurons (red box).

969

Figure 2. Firing traces of the four model cells in response to current injection (1 second). Note that APs are not explicitly modeled in I&F neurons. **A:** The somatic membrane voltage of the granule cell (GC) model in response to +90 pA (top), and -50 pA (bottom) somatic current injections. **B.** Same as in **A,** for the mossy cell (MC) with +300 pA (top) and -300pA (bottom) current injections. **C.** Same as in **A,** for the Basket cell (BC), with +200 pA (top) and -50 pA (bottom) current injections. **D.** Same as in **A,** for the HIPP cell, with +300 pA (top) and -50 pA (bottom) current injections. Current – Voltage (I-V) curves are given in Figure 2-figure supplement 1, while Current – frequency plots are shown in Figure 2-figure supplement 2. Moreover, Figure 2-figure supplement 3 shows the somatic EPSP against Arithmetic sum for GCs under control, pruning and growth conditions. In Figure 2-figure supplement 4 and 5, the corresponding EPSP vs. Arithmetic sum curves for GCs after matching R_{in} and sparsity are given, respectively.
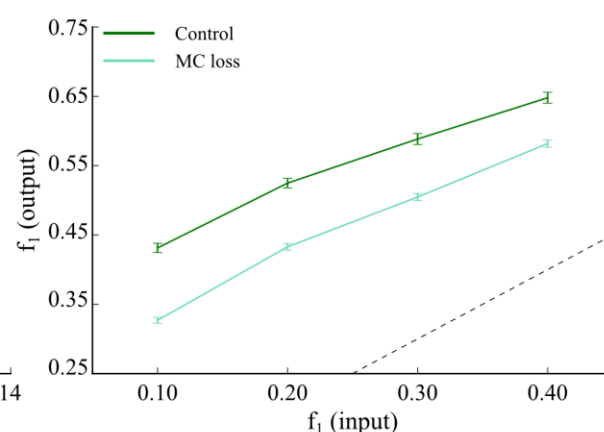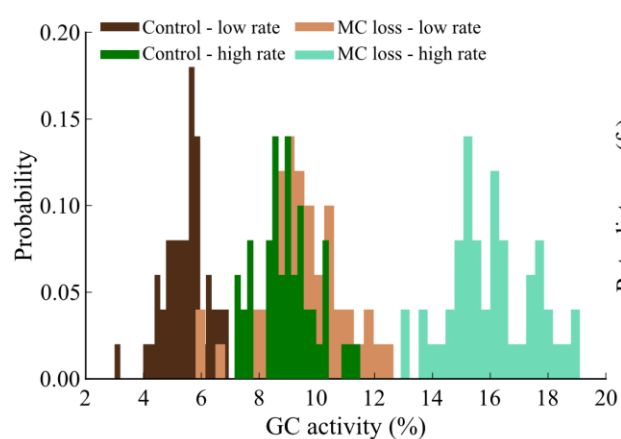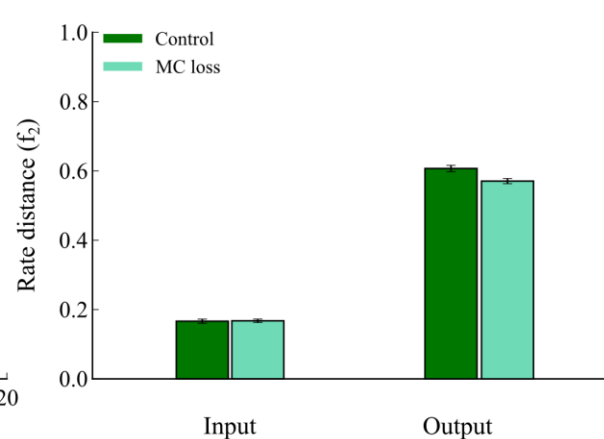
980
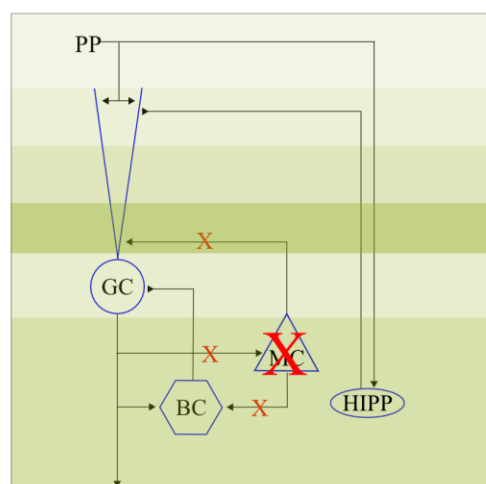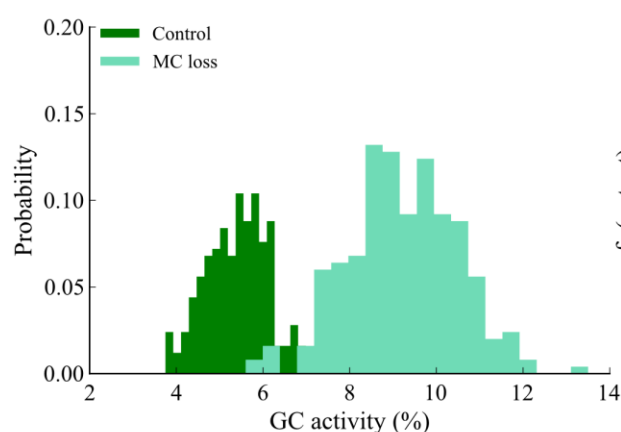
Figure 3. Complete mossy cell loss reduces pattern separation efficiency in the DG network. **A.** Schematic

representation of the 12-dendrite DG network with MC loss. **B.** The corresponding probability density functions of

GC activity in response to 40 Hz input for the control (dark green) and MC loss conditions (light green). The mean

984 activity is 5% and 9% for the control and MC loss networks, respectively. The respective mean firing rates of GCs

985 are shown in Table 3. The histograms were calculated with 20 bins each. **C.** Input / Output population distances

986 (f_1) for the control (dark green) and MC loss (light green) networks estimated using input patterns with increasing

987 similarity. The dashed line denotes the limit above which the model performs pattern separation. MC loss

988 reduces pattern separation efficiency for all input patterns tested. Error bars represent the standard error of the

989 mean (Erevitt and Skrondal, 2010). **D.** Probability density functions of GC activity using control and MC loss

990 models presented with two input patterns that differ only in their firing rates. Shades of green represent the high

991 frequency input (50 Hz), while shades of brown represent the low frequency input (40Hz). Dark and light shades

992 represent the control and MC loss condition, respectively. The respective mean firing rates of GCs are shown in

993 Table 3. **E.** Input / Output rate distances (f_2) for the control (dark green) and MC loss (light green) networks

994 estimated using two input patterns with different firing frequencies, 40 and 50 Hz respectively. MC loss slightly

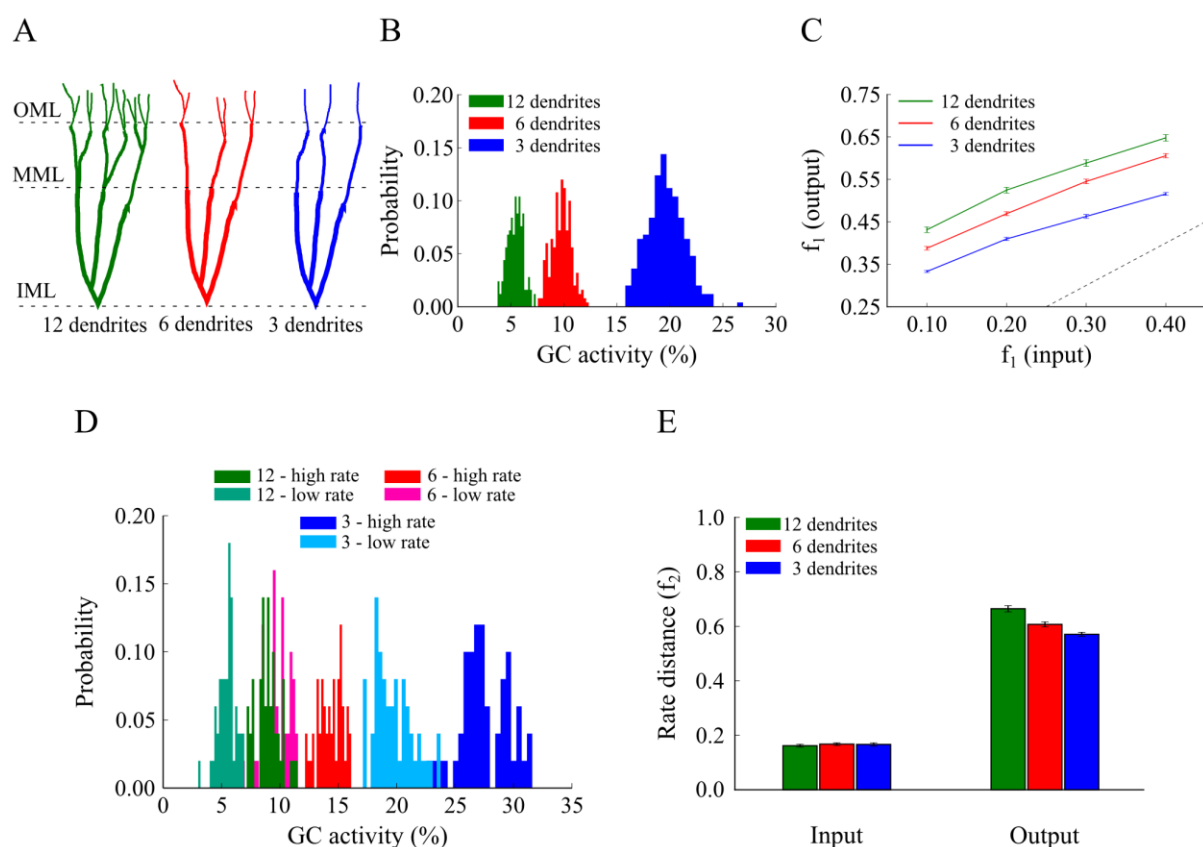995 reduces the efficiency of pattern separation.

45

Figure 4. Effect of GC dendrite pruning on pattern separation. **A**. A schematic drawing of the three GC models with 12, 6 and 3 dendrites. **B.** Corresponding probability density functions of GC activity for the three GC models in response to a single input pattern at 40 Hz. The mean activity is inversely analogous to the number of dendrites: as the number of dendrites decreases, the GC population becomes more active, i.e., less sparse. The respective mean firing rates of GCs are shown in Table 3. **C.** Input / Output population distances (f_1), for the 12-dendrite (green), 6-dendrite (red) and 3-dendrite (blue) GC models in response to the presentation of two overlapping input patterns at 40 Hz. Input pairs were generated so as to have decreasing amounts of overlap, as depicted in Figure 1B. The dashed line denotes the limit above which the model performs pattern separation. Performance declines as the dendritic tree has fewer dendrites. Error bars represent the standard error of the mean across trials. **D.** Probability density functions of GC activity for the three GC models in response to presentation of two input patterns with different firing rates (low rate = 40 Hz, high rate = 50 Hz), as depicted in Figure 1C. GC activity increases with the number of dendrites and the input firing rate. The respective mean firing rates of GCs are shown in Table 3. **E.** Input / Output rate distances (i.e., f_2) for the three models. All three models perform pattern separation, as the rate distances in the input are significantly higher than the corresponding ones in the output.
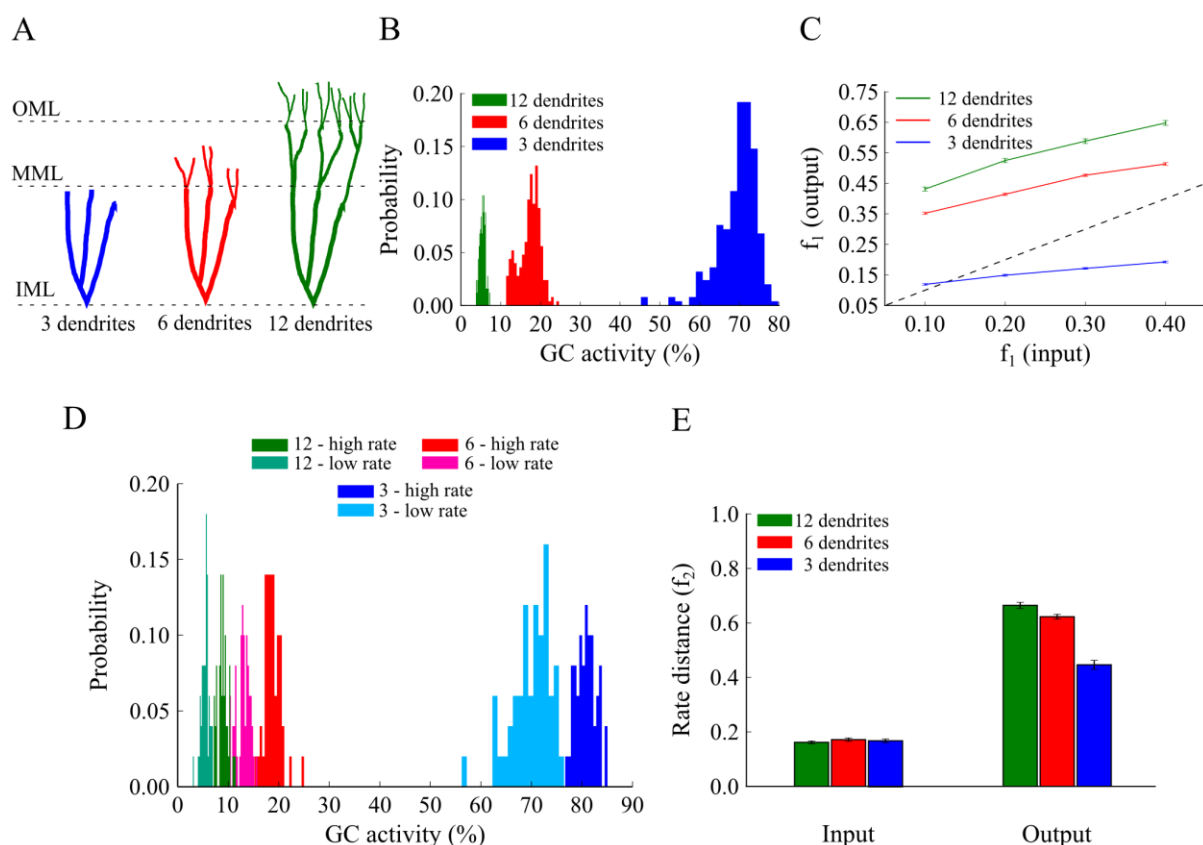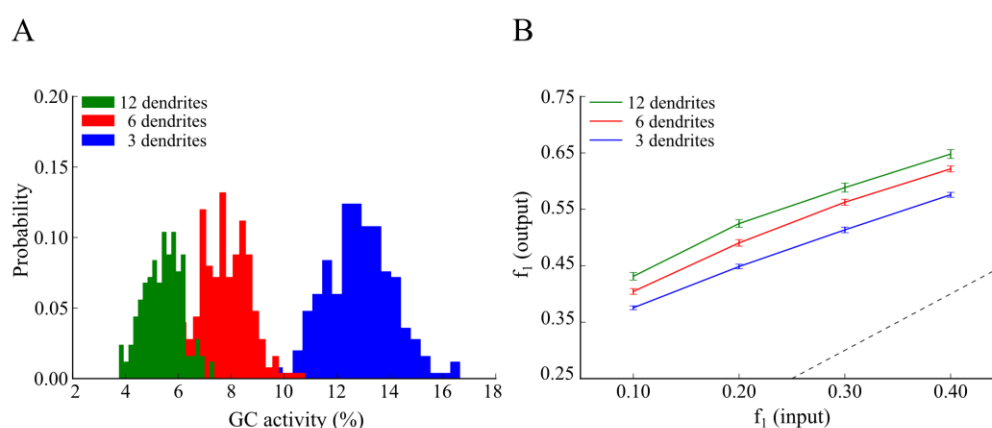
Figure 5. Effect of GC dendrite growth on pattern separation. **A**. A schematic drawing of the three GC models with 3, 6 and 12 dendrites. **B.** Corresponding probability density functions of GC activity for the three GC models in response to a single input pattern at 40 Hz. The mean activity is inversely analogous to the number/length of dendrites: as dendrites grow, the GC population becomes sparser, i.e., fewer GCs are active. The respective mean firing rates of GCs are shown in Table 3. **C.** Input / Output population distances (f_1), for the 3-dendrite (blue), 6-dendrite (red) and 12-dendrite (green) GC models in response to the presentation of two overlapping input patterns at 40 Hz, with different degrees of overlap, as depicted in Figure 1B. The dashed line denotes the limit above which the model performs pattern separation. Performance improves with the growth of dendrites. **D.** Probability density functions of GC activity for the three GC models in response to presentation of two input patters with different firing rates (low rate = 40 Hz, high rate = 50 Hz), as depicted in Figure 1C. GC activity decreases with the number of dendrites and increases with the input firing rate. The respective mean firing rates of GCs are shown in Table 3. **E.** Input / Output rate distances (i.e., f_2) for the three models. The number of GC dendrites is again analogous to the pattern separation performance.

47

Dendritic pruning
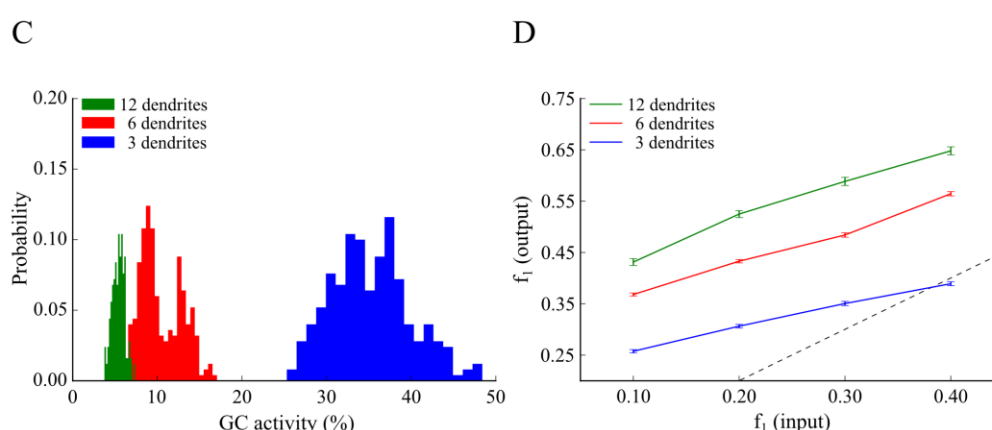

Dendritic growth

1026

Figure 6. Effect of GC dendritic pruning (top panel) and growth (bottom panel) on pattern separation when the input resistance (R_{in}) is the same across models. To match R_{in}, the leak conductance (g_{leak}) was increased by a factor of 1.695 and 1.230, in the 3- and 6-dendrite models respectively. **A.** Corresponding probability density functions of GC activity for the three GC models in response to a single input pattern at 40 Hz. GC activity distributions become more similar but remain inversely analogous to the number of dendrites: as the number of dendrites increase, the GC population becomes sparser. The respective mean firing rates of GCs are shown in Table 3. **B.** Input / Output population distances (f_1), for the 3-dendrite (blue), 6-dendrite (red) and 12-dendrite (green) GC models in response to the presentation of two overlapping input patterns at 40 Hz as depicted in Figure 1B. The dashed line denotes the limit above which the model performs pattern separation. Performance improves with the number of dendrites. **C.** The same as in **A.** for the growth experiment. While distributions move closer to one another, the inverse relationship between dendritic number and mean sparsity is preserved. **D.** Same as in **B.** for the growth experiment. Pattern separation efficiency still correlates with the number of dendrites. Figure 6-figure supplement 1 depicts the corresponding pattern separation efficiency based on 'rate distance'.
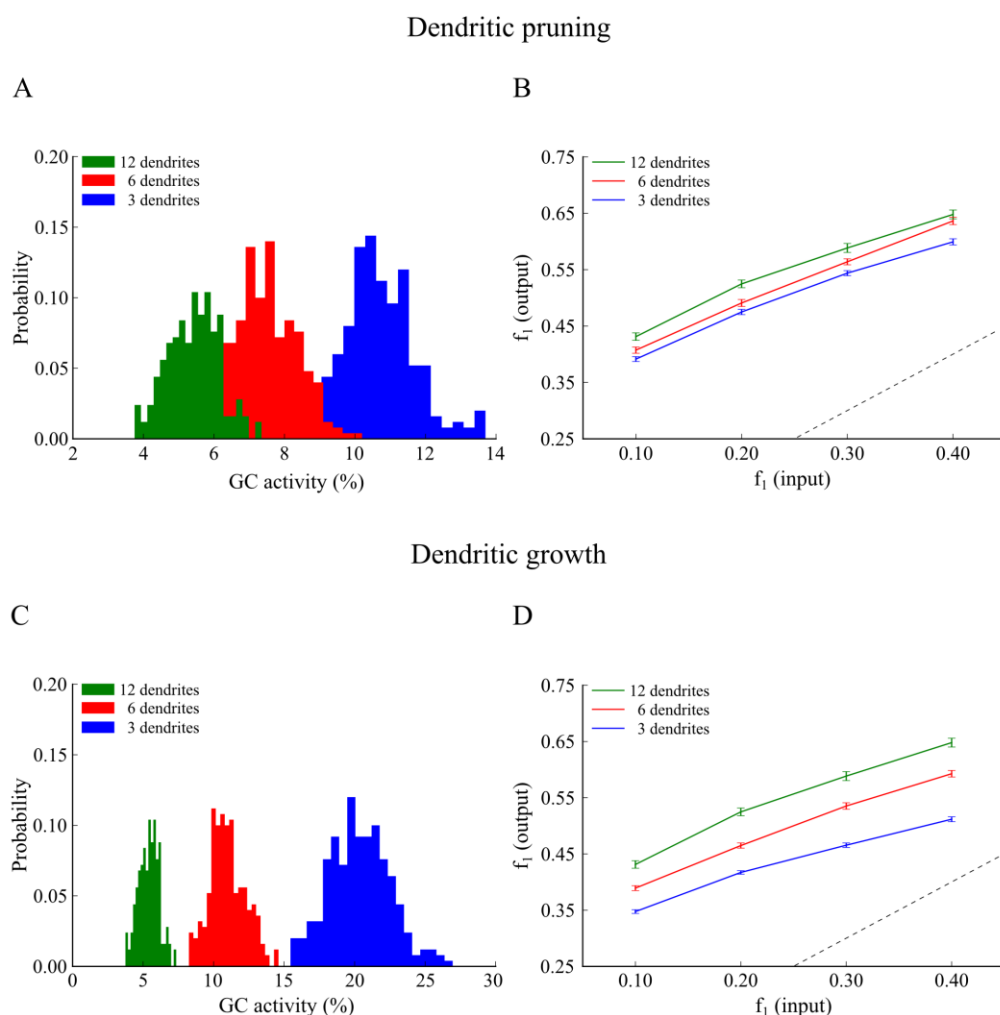
1041

Figure 7. Effect of GC dendritic pruning (top panel) and growth (bottom panel) on pattern separation when matching the input resistance (R_{in}) via increasing the somatic size. The neuronal soma of the 3- and 6-dendrite models was increased by a factor of 1.527 and 1.278, respectively. **A.** Corresponding probability density functions in response to a single input pattern at 40 Hz. While distributions move closer, the mean activity remains inversely analogous to the number of dendrites. The respective mean firing rates of GCs are shown in Table 3. **B.** Input / Output population distances (f_1), for the 3-dendrite (blue), 6-dendrite (red) and 12-dendrite (green) GC models in response to the presentation of two overlapping input patterns at 40 Hz as depicted in Figure 1B. The dashed line denotes the limit above which the model performs pattern separation. Performance becomes similar yet statistically different among the three corrected models and remains analogous to the number of dendrites. **C.** Same as in **A.** for the growth experiment. The inverse relationship between dendritic number and mean sparsity is preserved. **D.** Same as in **B.** for the growth experiment. Pattern separation efficiency remains different and analogous to the number of dendrites. Figure 7-figure supplement 1 depicts the corresponding pattern separation efficiency based on 'rate distance'.

49
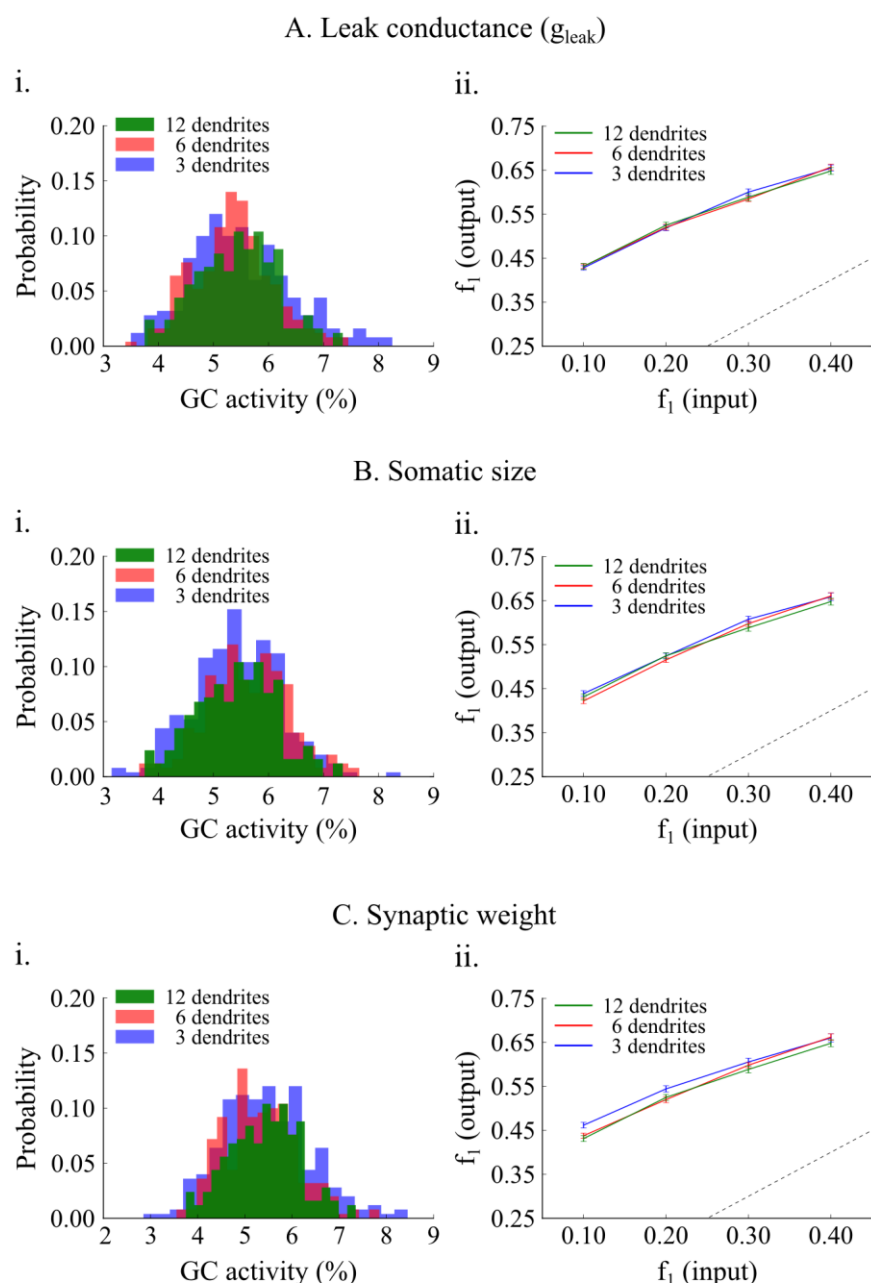
Figure 8. Effect of matching sparsity on pattern separation efficiency. **A.** The "leak" conductance, g_{leak}, of the 6- and 3-dendrite GC models increases by a factor of 1.58 and 2.48, respectively. **A.i** Resulting GC activity distributions are not statistically different. **A.ii** Networks with corrected GC models have identical performance. Differences in pattern separation using the population metric are not statistically significant. **B.** GC activity distributions are matched by increasing the soma diameter and length of the 6- and 3-dendrite GC models by 1.48 and 1.87, respectively. **B.ii** The network with corrected 3-dendrite GC models has a slightly smaller pattern separation efficiency compared to the other two probably because its activity distribution is wider. Generally the three models have very similar pattern separation performance. **C.** GC activity distributions are matched by decreasing the EC → GC synaptic weight from 1.00, to 0.75 and 0.56 in the 6-, and 3- dendrite models, respectively. Pattern separation efficiency is statistically the same across all corrected GC models.

1066
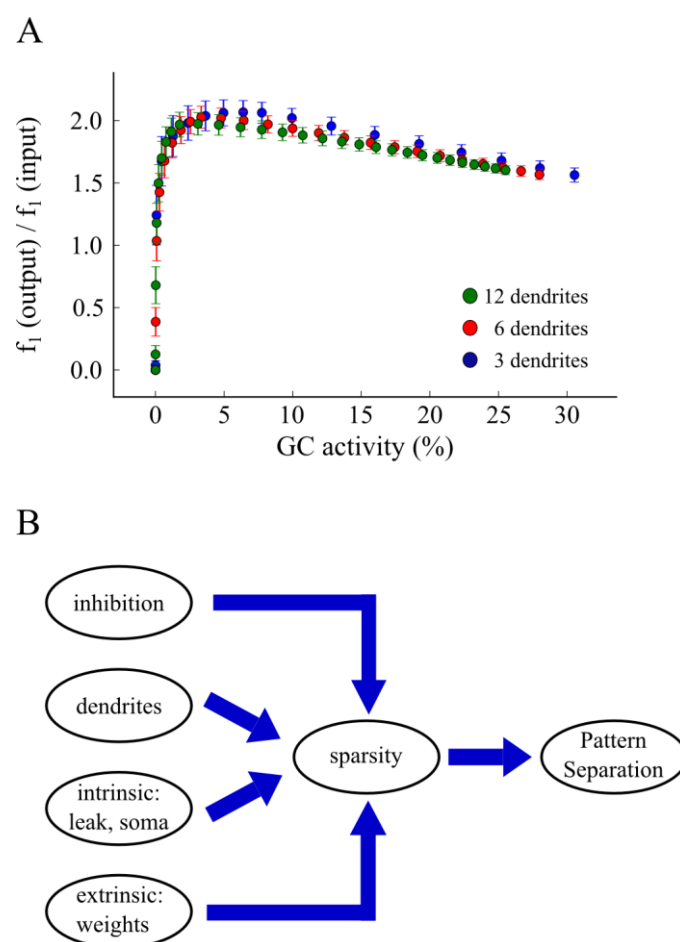
1067 **Figure 9. A.** The ratio of $f_{1(output)}$ to $f_{1(input)}$ for all three models as function of GC activity. Each dot represents

1068 an average of 20 trials for a specific synaptic weight value. We used values in the range of 0.0 to 25.0. For any

1069 given sparsity level, pattern separation efficiency is identical across all corrected GC models. **B.** Schematic

1070 representation of our proposed working hypothesis based on model predictions: sparsity is the key determinant of

1071 pattern separation. Sparsity is in turn controlled by a number of mechanisms, including inhibition, the presence of

1072 dendrites as well as various intrinsic and extrinsic mechanisms.

1073 # Tables

1074 **Table 1. Physiological properties of real and model neurons**

Cell type	Input resistance R_{in} (MΩ)		Membrane time constant, τ_m (ms)		Sag ratio		Maximum firing rate (Hz)	
	Model	Biological	Model	Biological	Model	Biological	Model	Biological
Granule cells	360	292 ± 34	41.2	31 ± 2	0.91	0.96 ± .1	60	70 ± 10
Mossy cells	105	199 ± 19	33.7	35 ± 5	0.98	0.81 ± .3	45	50 ± 6
Basket cells	55	56 ± 9	9.67	10 ± 1	0.99	0.97 ± .02	247	230 ± 15
HIPP cells	363	371 ± 47	21.4	15 ± 0	0.84	0.82 ± .04	113	101 ± 24
Biological value	Lubke et al., 1998, Krueppel et al., 2009		Lubke et al., 1997, Ratzliff et al., 2004		Lubke et al., 1998, Bartos et al., 2001		Lubke et al., 1997	

1075

1076   **Table 2. DG network (12-dendrite model) performance on a simple pattern separation task.**

Input Similarity ($f_{1(input)}$)	Output Similarity ($f_{1(output)}$) mean ± sem
0.10	0.43 ± 0.007
0.20	0.52 ± 0.007
0.30	0.59 ± 0.008
0.40	0.64 ± 0.008
Input Similarity ($f_{2(input)}$) mean ± sem	Output Similarity ($f_{2(output)}$) mean ± sem
0.16 ± 0.05	0.66 ± 0.01

1077

1078 **Table 3. Mean firing frequencies of GCs in response to the various input patterns used in**

1079 **Figures 3-8**

1080 *Population-distance Experiments (Pruning, Growth, MC loss)*

GC models	Mean firing rate ± sem (Hz)		
	Pruning	Growth	MC loss
12-dendrite	3.50±0.002	3.50±0.002	4.82±0.002
6-dendrite	3.65±0.009	3.85±0.007	-
3-dendrite	3.90±0.006	6.35±0.005	-

1081

1082 *Population-distance Experiments (Match R_{in})*

GC models	Mean firing rate ± sem (Hz)			
	Pruning		Growth	
	g_{leak}	Soma dimensions	g_{leak}	Soma dimensions
6-dendrite	3.61±0.009	3.58±0.009	3.66±0.008	3.60±0.008
3-dendrite	3.75±0.007	3.58±0.007	4.59±0.006	3.78±0.006

1083

1084 *Population-distance Experiments (Match sparsity)*

GC models	Mean firing rate ± sem (Hz)		
	g_{leak}	Soma dimensions	Synaptic weight
6-dendrite	3.47±0.010	3.44±0.010	3.31±0.010
3-dendrite	3.47±0.010	3.31±0.010	3.12±0.008

1085

1086 *Rate-distance Experiments (Control, Growth, MC loss)*

GC models	Mean firing rate ± sem (Hz)					
	Control		Growth		MC loss	
	Low input rate (40Hz)	High input rate (50Hz)	Low input rate (40Hz)	High input rate (50Hz)	Low input rate (40Hz)	High input rate (50Hz)
12-dendrite	3.75±0.036	5.24±0.048	3.75±0.036	5.24±0.048	4.94±0.057	8.07±0.110
6-dendrite	3.98±0.028	5.20±0.035	3.83±0.023	5.03±0.030	-	-
3-dendrite	4.13±0.019	5.48±0.023	6.43±0.015	9.07±0.017	-	-

1087

1088   **Table 4. Model parameters for all neuronal types**

Model Parameter	Granule cells		Mossy cells	Basket cells	HIPP cells
	Soma	dendrites			
E_l (mV) Resting potential	-87	-82	-64	-52	-59
g_l (nS) "Leak" conductance	0.00003[a]	0.00001[a]	4.53	18.054	1.930
C_m (nF) Membrane capacitance	1.0[b]	2.5[b]	0.621	0.1793	0.0584
V_{reset} (mV) Reset voltage	-74		-49	-45	-56
$V_T = V_{thr}$ (mV) Threshold voltage	-56		-42	-39	-50
Δ_T (mV) Slope factor	-		2	2	2
α (nS) Adaptation coupling parameter	2.0		2	0.1	0.82
τ_w (ms) Adaptation time constant	45		180	100	93
b (nS) Spike triggered adaptation	0.0450		0.0829	0.0205	0.015

1089   [a]For the GC model the "leak" conductance is given in Siemens/cm^2

1090   [b]For the GC model the membrane capacitance is given in uF/cm^2

1091 **Table 5. Morphological structure of GC models**

Structure of GC models	Control	Pruning		Growth	
	12 dendrites	**6 dendrites**	**3 dendrites**	**6 dendrites**	**3 dendrites**
# of compartments					
total	21	15	9	9	3
proximal	3	3	3	3	3
medial	6	6	3	6	-
distal	12	6	3	-	-
length per compartment (um)	83	83	83	83	83
total dendritic length (um)	1743	1245	747	747	249
diameter per compartment (um)					
proximal	1.0	1.0	1.0	1.0	1.0
medial	0.9	0.9	0.9	0.9	-
distal	0.8	0.8	0.8	-	-

1092

1093　**Table 6. Synaptic parameters of the dentate network**

From (column) / To (row)	Granule cells	Mossy cells	Basket cells	HIPP cells
AMPA				
Perforant Path				
g_{max} (nS)	0.8066			0.240
τ_{rise} (ms)	0.1			2.0
τ_{decay} (ms)	2.5			11.0
delay (ms)	3.0			3.0
Granule cells				
g_{max} (nS)		0.500	0.210	
τ_{rise} (ms)		0.5	2.5	
τ_{decay} (ms)		6.2	3.5	
delay (ms)		1.5	0.8	
Mossy cells				
g_{max} (nS)	0.1066		0.350	
τ_{rise} (ms)	0.1		2.5	
τ_{decay} (ms)	2.5		3.5	
delay (ms)	3.0		3.0	
NMDA				
Perforant Path				
g_{max} (nS)	0.8711			0.276
τ_{rise} (ms)	0.33			4.8
τ_{decay} (ms)	50.0			110.0
delay (ms)	3.0			3.0
Granule Cells				
g_{max} (nS)		0.525	0.231	
τ_{rise} (ms)		4.0	10.0	
τ_{decay} (ms)		100.0	130.0	
delay (ms)		1.5	0.8	
Mossy Cells				
g_{max} (nS)	0.1151		0.385	
τ_{rise} (ms)	0.33		10.0	
τ_{decay} (ms)	50.0		130.0	
delay (ms)	3.0		3.0	
GABA$_A$				
Basket cells				
g_{max} (nS)	14.0			
τ_{rise} (ms)	0.9			
τ_{decay} (ms)	6.8			
delay (ms)	0.85			
HIPP cells				
g_{max} (nS)	0.12			
τ_{rise} (ms)	0.9			
τ_{decay} (ms)	6.8			
delay (ms)	1.6			

1094